Delft University of Technology

Probing the Innermost Regions of AGN Jets and Their Magnetic Fields with RadioAstron. V. Space and Ground Millimeter-VLBI Imaging of OJ 287

Gómez, José L.; Traianou, Efthalia; Krichbaum, Thomas P.; Lobanov, Andrei P.; Fuentes, Antonio; Lico, Rocco; Zhao, Guang Yao; Bruni, Gabriele; Gurvits, Leonid I.; More Authors

CrossMark

Probing the Innermost Regions of AGN Jets and Their Magnetic Fields with RadioAstron. V. Space and Ground Millimeter-VLBI Imaging of OJ 287

José L. Gómez[1] , Efthalia Traianou[1,2] , Thomas P. Krichbaum[2] , Andrei P. Lobanov[2,3] , Antonio Fuentes[1] ,
Rocco Lico[1,2,4] , Guang-Yao Zhao[1] , Gabriele Bruni[5] , Yuri Y. Kovalev[2,3,6] , Anne Lähteenmäki[7,8] , Petr A. Voitsik[6] ,
Mikhail M. Lisakov[2,6] , Emmanouil Angelakis[9] , Uwe Bach[2] , Carolina Casadio[10,2] , Ilje Cho[1] , Lankeswar Dey[11] ,
Achamveedu Gopakumar[11] , Leonid I. Gurvits[12,13] , Svetlana Jorstad[14,15] , Yuri A. Kovalev[6] , Matthew L. Lister[16] ,
Alan P. Marscher[14] , Ioannis Myserlis[17,2] , Alexander B. Pushkarev[6,18] , Eduardo Ros[2] , Tuomas Savolainen[2,7,8] ,
Merja Tornikoski[7] , Mauri J. Valtonen[19,20] , and Anton Zensus[2]

[1] Instituto de Astrofísica de Andalucía-CSIC, Glorieta de la Astronomía s/n, E-18008 Granada, Spain
[2] Max-Planck-Institut für Radioastronomie, Auf dem Hügel 69, D-53121 Bonn, Germany
[3] Moscow Institute of Physics and Technology, Institutsky per. 9, Dolgoprudny, Moscow region, 141700, Russia
[4] INAF—Istituto di Radioastronomia, via Gobetti 101, I-40129 Bologna, Italy
[5] INAF—Istituto di Astrofisica e Planetologia Spaziali, via Fosso del Cavaliere 100, I-00133 Roma, Italy
[6] Lebedev Physical Institute of the Russian Academy of Sciences, Leninsky prospekt 53, 119991 Moscow, Russia
[7] Aalto University Metsähovi Radio Observatory, Metsähovintie 114, FI-02540 Kylmälä, Finland
[8] Aalto University Department of Electronics and Nanoengineering, PL15500, FI-00076 Aalto, Finland
[9] Section of Astrophysics, Astronomy & Mechanics, Department of Physics, National and Kapodistrian University of Athens, Panepistimiopolis Zografos 15784, Greece
[10] Institute of Astrophysics, Foundation for Research and Technology, Hellas, Voutes, 70013 Heraklion, Greece
[11] Department of Astronomy and Astrophysics, Tata Institute of Fundamental Research, Mumbai 400005, India
[12] Joint Institute for VLBI ERIC (JIVE), Oude Hoogeveensedijk 4, 7991 PD Dwingeloo, The Netherlands
[13] Aerospace Faculty, Delft University of Technology, Kluyverweg 1, 2629 HS Delft, The Netherlands
[14] Institute for Astrophysical Research, Boston University, 725 Commonwealth Avenue, Boston, MA 02215, USA
[15] Astronomical Institute, St. Petersburg State University, Universitetskij, Pr. 28, Petrodvorets, St. Petersburg 198504, Russia
[16] Department of Physics and Astronomy, Purdue University, 525 Northwestern Avenue, West Lafayette, IN 47907, USA
[17] Institut de Radioastronomie Millimétrique, Avenida Divina Pastora, 7, Nucleo Central, E-18012 Granada, Spain
[18] Crimean† Astrophysical Observatory, 98409 Nauchny, Crimea, Russia
[19] Finnish Centre for Astronomy with ESO, University of Turku, FI-20500 Turku, Finland
[20] Department of Physics and Astronomy, University of Turku, FI-20500 Turku, Finland

Abstract

We present the first polarimetric space very long baseline interferometry (VLBI) observations of OJ 287, observed with RadioAstron at 22 GHz during a perigee session on 2014 April 4 and five near-in-time snapshots, together with contemporaneous ground VLBI observations at 15, 43, and 86 GHz. Ground-space fringes were obtained up to a projected baseline of 3.9 Earth diameters during the perigee session, and at a record 15.1 Earth diameters during the snapshot sessions, allowing us to image the innermost jet at an angular resolution of $\sim 50\,\mu$as, the highest ever achieved at 22 GHz for OJ 287. Comparison with ground-based VLBI observations reveals a progressive jet bending with increasing angular resolution that agrees with predictions from a supermassive binary black hole model, although other models cannot be ruled out. Spectral analyses suggest that the VLBI core is dominated by the internal energy of the emitting particles during the onset of a multiwavelength flare, while the parsec-scale jet is consistent with being in equipartition between the particles and magnetic field. Estimated minimum brightness temperatures from the visibility amplitudes show a continued rising trend with projected baseline length up to 10^{13} K, reconciled with the inverse-Compton limit through Doppler boosting for a jet closely oriented to the line of sight. The observed electric vector position angle suggests that the innermost jet has a predominantly toroidal magnetic field, which, together with marginal evidence of a gradient in rotation measure across the jet width, indicates that the VLBI core is threaded by a helical magnetic field, in agreement with jet formation models.

Unified Astronomy Thesaurus concepts: Active galactic nuclei (16); Extragalactic magnetic fields (507); Relativistic jets (1390); Polarimetry (1278); Blazars (164); Magnetic fields (994); Quasars (1319); Radio astronomy (1338); Very long baseline interferometry (1769); Space telescopes (1547); Plasma jets (1263); Radio cores (1341)

1. Introduction

The BL Lacertae object OJ 287 (0851+202, $z = 0.306$; Stickel et al. 1989) is considered to be one of the most remarkable examples of an active galactic nucleus (AGN). The 12 yr quasiperiodic outbursts in the optical regime, often accompanied by multiwavelength flaring activity, are attributed to the existence of a supermassive binary black hole (SMBBH) system, hidden in its compact center (Sillanpää et al. 1988; Valtonen et al. 2016, and references thereafter). OJ 287, which has a well-aligned with our line-of-sight radio jet, has shown very remarkable behavior in the past. During the period 2004–2006, Agudo et al. (2012) reported an erratic jet-swing by almost 100°, attributed to asymmetric

accretion flow to the central engine. Systematic jet-axis rotation has been observed by Cohen (2017a) and Britzen et al. (2018), describing a 24–30 yr rotation cycle of a helical jet, explained by either the Lense–Thirring effect introduced by the wobbling of the accretion disk around the primary black hole (BH), or precession induced by the binary companion (Lense & Thirring 1918; Thirring 1918).

The elucidation of the origin and the phenomenology of relativistic jets emanating from SMBBH belongs to the frontiers of modern astronomical research. Some theoretical models suggest that relativistic AGN jets can be driven by strong magnetic fields anchored on the BHs accretion disk (Blandford & Payne 1982). Other scenarios suggest that jets are driven by the conversion of the rotational energy of the BH to Poynting flux via the open magnetic field lines, which are attached to the BH ergosphere (Blandford & Znajek 1977). In reality, superposition of both mechanisms is also possible (e.g., Chiaberge et al. 2000). Close to the central engine, the plasma flow is accelerated and collimated under the presence of a coiled magnetic field. Under such extreme conditions, the dynamics and the stability of the relativistic plasma flow can be strongly influenced by disruptions of the accretion flow, pressure mismatches between the jet and the ambient medium, as well as within the jet itself, leading to the formation of moving shocks, standing shocks, and instabilities (Gómez et al. 1997; Komissarov & Falle 1997; Begelman 1998; Aloy et al. 2003).

Very long baseline interferometry (VLBI) is a powerful technique that allows us to achieve the angular resolution needed to resolve and study the fine structure of extragalactic jets. By increasing the observed frequency or the baseline length of the array elements, one can probe jet features located in a region of tens of Schwarzschild radii away from the supermassive black hole (SMBH), and ultimately using millimeter wavelengths (Boccardi et al. 2017) achieve the necessary resolution that has enabled the Event Horizon Telescope Collaboration to obtain the first image of a BH shadow in M87 (EHT Collaboration et al. 2019a, 2019b, 2019c, 2019d, 2019e, 2019f; EHT Collaboration et al. 2021a, 2021b). Besides VLBI observations in total intensity, polarimetric observations are essential (Gómez et al. 2001). They constitute a powerful tool for deriving fundamental constraints on jet physics and magnetic field configuration.

The images we obtain via VLBI observations allow us to illustrate the relativistic plasma flow and trace distinct features known as blobs or knots. These features usually emerge from the bright and typically unresolved end of the radio jet, known as the core. The nature of this feature differs from that of the real jet base, and it is not always easily determined. As also described in Marscher (2008), what we see as the VLBI core can correspond to the surface where the opacity (τ_ν) reaches unity (Blandford & Königl 1979), or to a standing shock, which is located downstream of the $\tau_\nu = 1$ surface (Daly & Marscher 1988; Gómez et al. 1995; Mizuno et al. 2015). The true nature of OJ 287 VLBI core is still unexplored.

The RadioAstron space VLBI mission (Kardashev et al. 2013), led by the Russian Astro Space Center and the Lavochkin Scientific and Production Association, operated between 2011 and 2019. It featured a 10 m radio telescope on board the Spektr-R satellite and was equipped with receivers operating 0.32 GHz (P band), 1.6 GHz (L band, dual polarization), 4.8 GHz (C band), and 22 GHz (K band, dual polarization). With an apogee of ~350,000 km, space VLBI

observations with RadioAstron are capable of imaging blazar jets in total and linearly polarized intensity with an unprecedented resolution of the order of few tens of microarcseconds (μas) when observing at the shorter wavelengths (e.g., Gómez et al. 2016).

Three Key Science Programmes on AGN imaging have collected data since 2013 to study the launching, collimation, and magnetic field properties of AGN jets (e.g., Zensus AdSPR on strong sources program), while the AGN survey studied the brightness temperature of their cores (e.g., Kovalev et al. 2016, 2020). The RadioAstron Polarization KSP has collected data throughout the whole duration of the space VLBI mission, and is aimed to probe the innermost jet regions and their magnetic field in a sample of the most energetic blazars. Results from the RadioAstron Polarization KSP are reported for 0642+449 in Lobanov et al. (2015), BL Lac in Gómez et al. (2016), 0716+714 in Kravchenko et al. (2020), 3C 345 in Pötzl et al. (2021), and 3C 273 in Bruni et al. (2017) and Bruni et al. (2021). Here we present the first RadioAstron observations of OJ 287 performed in 2014 at 22 GHz, in combination with quasi-simultaneous ground VLBI observations at 15, 22, 43, and 86 GHz.

The structure of this article is as follows. In Section 2, we present the multifrequency data set and the data reduction techniques. In Section 3 we report on the results from the VLBI study and discuss their implications in Section 4. Throughout this paper we have adopted the following cosmological parameters: $\Omega_M = 0.27$, $\Omega_\Lambda = 0.73$, and $H_0 = 71 \, \text{km s}^{-1} \, \text{Mpc}^{-1}$ (Komatsu et al. 2009), which result for OJ 287 in a luminosity distance of $D_L = 1.577$ Gpc and angular scale of 4.48 pc mas^{-1}.

2. Observations and Data Analysis

OJ 287 was observed with RadioAstron in 2014 as part of our Polarization KSP. In this section we describe the Radio-Astron observations and data analysis, as well as other close-in-time ground-based VLBI observations at multiple wavelengths. These include global millimeter VLBI array (GMVA) observations, archival 15 GHz VLBA data, and publicly available 43 GHz data from the VLBA-BU-BLAZAR monitoring program. A summary of the RadioAstron and GMVA observations, as well as the used archival data is provided in Table 1.

2.1. RadioAstron Space VLBI Observations at 22 GHz

The bright blazar OJ 287 was observed with RadioAstron on 2014 April 4–5 (from 12:00 to 03:45 UT, observing code GA030E) at a frequency of 22.236 GHz combining a 15:45 hr session during the perigee of the spacecraft (total RadioAstron on-source time was 6.3 hr). These imaging observations were supplemented by five short (between half an hour and 2 hr long) sessions on 2014 March 9, 10, 16, 27, and April 18 within the RadioAstron AGN survey program (Kovalev et al. 2020).

The RadioAstron perigee-imaging session of OJ 287 in 2014 April 4–5 was carried out with a ground array of 12 antennas, as listed in Table 1. The long-baseline snapshot sessions were conducted on 2014 March 9 (01:00 to 02:00 UT, at a projected baseline of 15.1 Earth diameters, $D_\oplus$), March 10 (01:00 to 02:00 UT, 5.8 $D_\oplus$), March 16 (2:15 to 03:00 UT, 15.1 $D_\oplus$), March 27 (00:00 to 00:25 UT, 4.6 $D_\oplus$), and April 18 (00:00 to 01:00 UT, 9.9 $D_\oplus$), all during different orbits of the Space

Table 1
RadioAstron and Complementary VLBI Observations of OJ 287 in 2014

ν_{obs} [GHz]	Instrument	Observation Date	Participating Antennas
(1)	(2)	(3)	(4)
15	VLBA	5 May	VLBA[c]
22[a]	RadioAstron	4 April	SRT+KVN+KL+ON+SH +TR+HH+NT+EF+YS+GB
43[b]	VLBA	3 May	VLBA[c]
86	GMVA	24 May	VLBA[d]+PV+EB+ON+PB

Note.

[a] RadioAstron perigee-imaging session; see the text for a description of complementary RadioAstron long-baseline visibility tracking sessions.
[b] Data from the VLBA-BU-BLAZAR monitoring program.
[c] North Liberty (NL) did not participate.
[d] Excluding Hancock (HN) and Saint Croix (SC) antennas, which do not have 86 GHz receivers. Antennas and VLBI array acronyms: VLBA—Very Long Baseline Array; KVN—Korean VLBI Network, comprising the array elements KT, KU, and KY; KL—Kalyazin; ON—Onsala; SH—Sheshan; TR—Torun; HH—Hartebeesthoek; NT—Noto; EF/EB—Effelsberg; YS—Yebes; GB—Green Bank; PV—Pico Veleta; PB—Plateau de Bure. Columns from left to right: (1) Observing frequency, (2) VLBI array, (3) Dates of data collection, (4) Array elements that participated in the observations.

Radio Telescope (SRT) than that of the main perigee-imaging session. Fringes to the SRT were found only with the Green Bank telescope for all of the snapshot sessions except the one on 2014 March 27, for which fringes were found only to Effelsberg. Signal-to-noise ratio (S/N) values of these long-baseline fringes lie in a range from 10 to 20. This is expected, as baseline sensitivity depends on size of the antennas and baseline projection, resulting in no fringe detection for the smaller antennas in our array in the long-baseline snapshots.

The imaging data were recorded in both left (LCP) and right (RCP) circular polarizations, with a total bandwidth of 32 MHz per polarization, split into two intermediate frequency (IF) bands. The SRT data were recorded by the RadioAstron satellite tracking station in Pushchino, including extended gaps of approximately 1 hr duration to allow for cooling of the onboard data downlink radio instrumentation of the *Spektr-R* satellite. The data of the five snapshot survey sessions were recorded in LCP only.

The imaging data were processed using the RadioAstron-dedicated version of the DiFX software correlator (Bruni et al. 2016), developed at the Max-Planck-Institut für Radiostronomie. After setting the ground stations clocks, we performed fringe fitting between the largest antennas of the ground array and RadioAstron, separately for each scan involving it. Such a process allows us to minimize the effects of the spacecraft acceleration terms along the considered orbit segment, by re-centering the signal in the correlation window every few minutes of observations. For scans giving no fringes (on the largest baselines), we estimated clock values by extrapolating them from successful scans on shorter space baselines. This provides a first-order value for fringes delay and rate, which can be later refined with the post-processing data reduction software.

The data of the long-baseline snapshot survey sessions were processed by the software correlator developed at the Astro Space Center of Lebedev Physical Institute in Moscow (Likhachev et al. 2017).
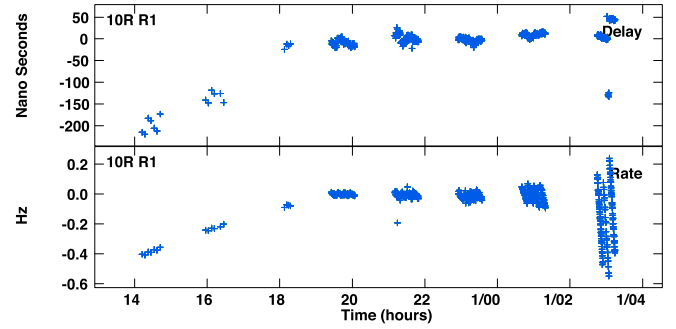

Figure 1. Residual delay (top) and rate (bottom) solutions for the SRT during the perigee-imaging session on 2014 April 4–5. Note the rapidly changing rate solutions associated with the acceleration of the SRT during the perigee near the end of the observations.

2.1.1. Initial Data Processing and Imaging

The initial data reduction of the correlated data was performed with NRAO's AIPS software package (Greisen 1990). This includes a priori amplitude calibration using the measured system temperatures for the ground antennas and the SRT. Opacity corrections as a function of source elevation were introduced for the ground telescopes, as well as parallactic angle corrections.

Fringe fitting of the imaging data was performed first by solving for the instrumental phase and single band delays of the SRT on a scan near the perigee of the SRT, providing the best fringe solutions for the ground-space baselines. This was followed by a global fringe search to solve for the residual delays and rates of the ground antennas only. Once the ground array was calibrated, fringe fitting of the SRT was performed by performing a baseline stacking of the ground array, and setting an exhaustive baseline search with the most sensitive ground antennas. Both polarizations and IFs were combined to maximize the sensitivity for ground-space fringe detection.

Figure 1 shows the residual delay and rate fringe solutions for the SRT corresponding to the perigee-imaging session. The strong ground-space fringes present during the perigee passing of the SRT near the end of the observations allowed for solution intervals as short as 10 s, capturing the quickly evolving fringe rates due to the SRT acceleration. Progressively larger solution intervals, up to four minutes, were used to increase the sensitivity on the longer projected baseline lengths to the SRT at the beginning of the experiment.

Fringes to the SRT were found throughout the whole duration of the perigee-imaging session, up to projected baselines of 3.9 Earth diameters in length. The group delay difference between the two polarizations was corrected using the AIPS task RLDLY, and a final complex bandpass function was solved for the receivers before averaging the fringe-fitted data in frequency across each IF and exporting for subsequent imaging.

Fringe fitting, complex bandpass calibration, and a priori amplitude calibration of the long-baseline snapshot survey data were performed using PIMA software (Petrov et al. 2011) as part of the pipeline data processing of the RadioAstron AGN survey (Kovalev et al. 2020).

The resulting coverage of the fringe-fitted data in the Fourier domain for the perigee-imaging session and the long-baseline snapshots is shown in Figure 2.

Imaging was performed using the DIFMAP software (Shepherd 1997) following the standard CLEAN (Högbom 1974)
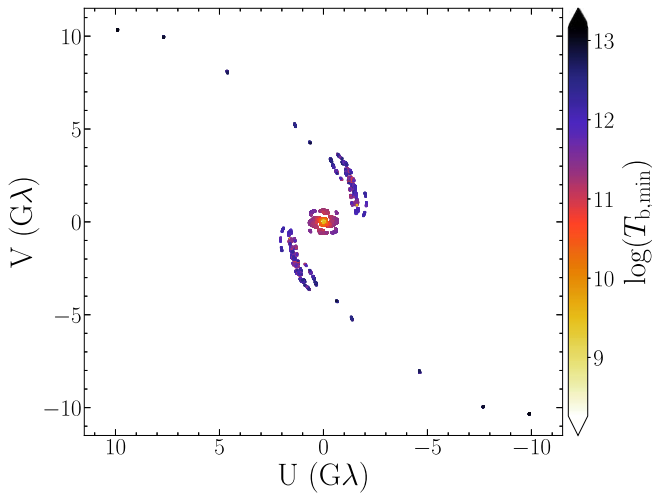
Figure 2. Fourier coverage of the fringe-fitted interferometric visibilities of OJ 287, observed by RadioAstron between 2014 March and April at 22 GHz. The color range designates the lower limit of the observed brightness temperature (see Section 3.5).

Figure 3. Self-calibrated visibility amplitudes and phases as a function of uv-distance of the RadioAstron observations of OJ 287 on 2014 March–April at 22 GHz. Over-plotted in red is the fit to these data of the CLEAN model obtained from the hybrid mapping using only the data collected during the perigee session, with fringe detections up to a projected baseline length of 3.9 Earth diameters (yellow dotted–dashed line). Detections at larger baseline spacing correspond to the long-baseline snapshots. The black dotted–dashed line separates the ground-only baselines from those obtained to the SRT.

hybrid imaging and self-calibration procedure. Only data from the perigee session (see Figure 3) were used for the imaging of the RadioAstron observations. Data from the long-baseline snapshots were excluded based on two arguments. First, no visibility closure quantities that could constrain the imaging and self-calibration procedure were obtained during the long-baseline snapshots, for which only single-baseline fringe detection were obtained. Second, the VLBI aperture synthesis technique is based on the assumption that the source remains stationary during the whole integration period being considered. This is no longer valid when considering together the perigee-imaging session and the long-baseline snapshots, conducted during different orbits of the SRT (weeks apart), and coincident with a high-activity period in the source, as discussed in Section 3.2. This is particularly relevant for the extremely small spatial scales probed during the long-baseline snapshots, with fringe detection spacing between 4.6 $D_\oplus$ and 15.1 $D_\oplus$. Although the long-baseline snapshot data were not used for the imaging of the RadioAstron data, they provide very valuable information regarding the brightness temperature at the smallest spatial scales, which is analyzed in Section 3.5.

Perigee-imaging self-calibrated Stokes I visibility amplitudes and phases as a function of Fourier spacing (uv-distance), and CLEAN model fit to these data are shown in Figure 3, where we also plot the long-baseline complex visibilities for comparison (see Section 3.5 for further discussion). Space VLBI fringes to the SRT extend the projected baseline spacing during the perigee-imaging session up to $\sim 3.9 D_\oplus$, increasing accordingly the angular resolution with respect to that provided by ground-based arrays up to $\sim 56\,\mu$as for uniform visibility weighting. RadioAstron images of OJ 287 during our 2014 April observations are shown in the right panels of Figure 4. In this figure we also show for reference the *over-resolved* image obtained by down-weighting the short baselines and using a Gaussian beam with FWHM equal to the nominal resolution of $\sim 12\,\mu$as corresponding to the longest projected baseline detection of $\sim 15.1\,D_\oplus$ obtained during the long-baseline snapshots, although we stress that these data were not used during the imaging process.

Calibration of the instrumental polarization and absolute orientation of the polarization vectors is discussed in Appendix A.1.
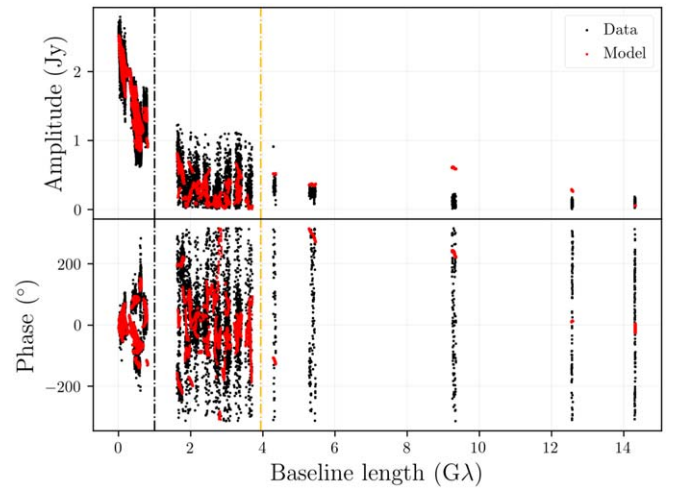
2.2. Complementary Ground VLBI Observations at 15, 43, and 86 GHz

We complement the analysis of the space VLBI observations of OJ 287 at 22 GHz with data from three ground-based interferometric observations performed at 15, 43, and 8 GHz within less than 2 months from the RadioAstron observations (see Table 1 and and Table 2). At 15 GHz, a single epoch of fully calibrated visibilities is provided via the publicly available database of the long-term monitoring MOJAVE program[21] (Lister et al. 2009; Principal investigator: J. L. Richards, project code S6407B). The data set at 43 GHz is part of the VLBA-BU-BLAZAR program[22], which includes monthly observations of 38 radio and γ-ray bright AGNs. The 43 GHz visibilities data available online are fully self-calibrated, following the analysis described in Jorstad et al. (2017).

The 86 GHz data were obtained from an observation made on May 25 with the GMVA. The duration of each scan was 8 minutes. The data were recorded at 2 Gbps rate (512 MHz bandwidth) with 2 bit digitization, apart from for Plateau de Bure observatory, which recorded at 1 Gbps rate mode and Yebes telescope that was equipped with only LCP receiver. During the correlation procedure, a polyphase filter band technology was used, segmented data into 16 IFs of 32 MHz bandwidth (eight physical IFs) per polarization. The data were correlated with the DiFX correlator (Deller et al. 2007) at the Max-Planck-Institut für Radioastronomie in Bonn, Germany.

Data reduction of the GMVA observations was performed using NRAO's AIPS software. We first applied the parallactic angle correction, followed by the determination of the inter-band phase and delay offsets between the intermediate frequencies, and the phase alignment across the observing band (known also as manual phase calibration). Next, a global fringe fitting was performed, correcting for the residual delays and phases with respect to a chosen reference antenna. The visibility amplitudes
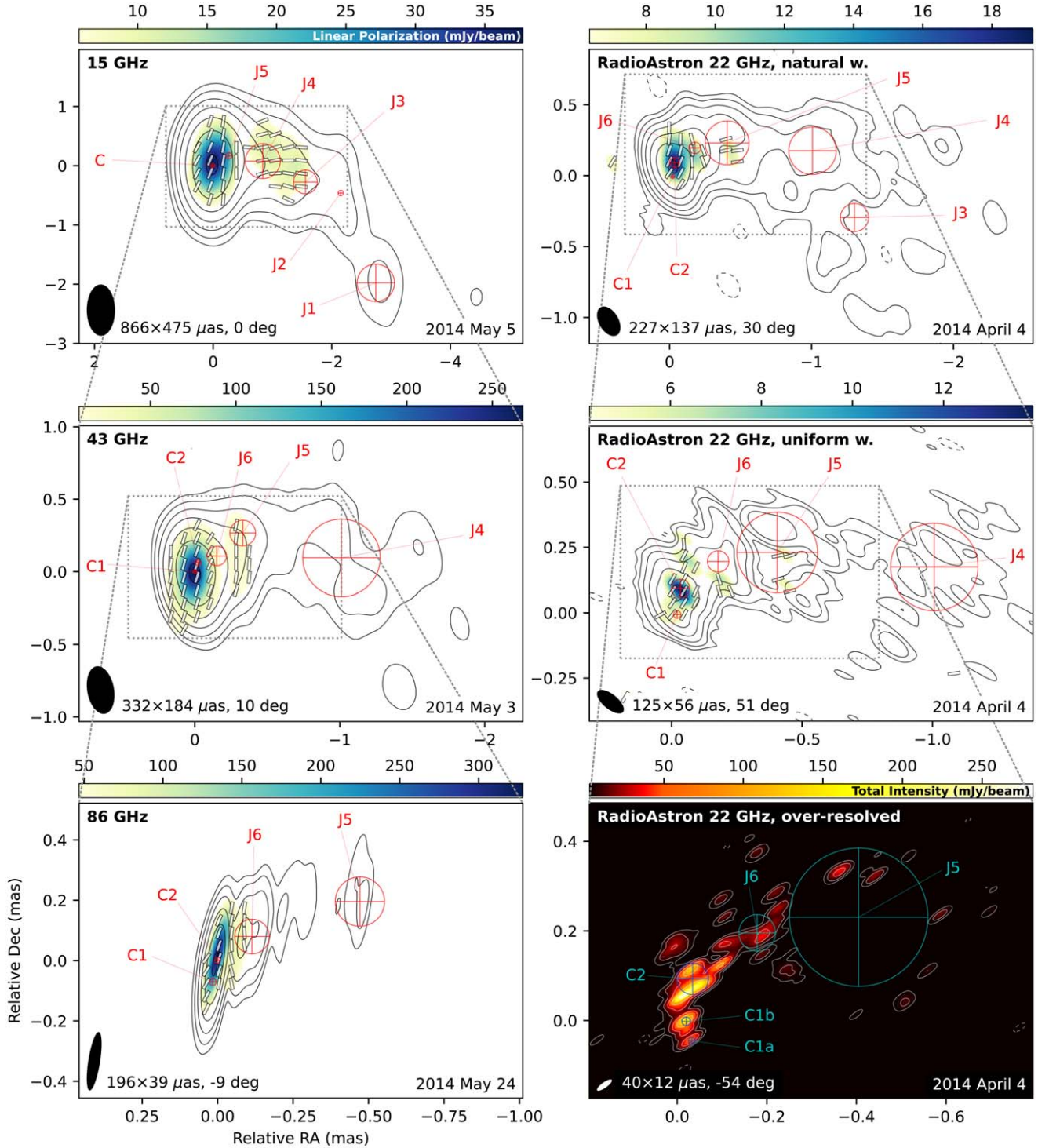

Figure 4. From top to bottom, left column: 15, 43, and 86 GHz polarimetric images obtained in 2014 May. Right column: RadioAstron 22 GHz polarimetric space VLBI images obtained with natural and uniform weighting in 2014 April. The *over-resolved* total intensity RadioAstron image at the nominal resolution corresponding to the maximum projected baseline fringe detection during the long-baseline snapshots is also shown for reference. Total intensity contours, EVPAs, and model-fit components are over-plotted. The lowest contours are ±10 and ±9 times the rms level (see Table 2) for the 86 GHz and RadioAstron over-resolved images, respectively, and ±7 for the remaining images, with successive contours in factors of three up to 90% of the total flux density peak. Synthesized beams and their parameters are located in the bottom-left corner of each map.

were calibrated, considering the contribution of atmospheric opacity effects based on the measured system temperatures and the gain-elevation curves of each telescope. Finally, the a priori calibrated data were exported to `DIFMAP` for subsequent imaging following the usual CLEAN and self-calibration procedure. The absolute EVPA calibration, as well as the leakage calibration method, is described in Appendix A.2.

2.3. Visibility Model Fitting

We modeled the observed brightness distribution in the jet of OJ 287 with two-dimensional Gaussian components in the visibility plane using the `DIFMAP` package and following the procedure described in Traianou et al. (2020). The imaging and modeling of the multifrequency VLBI data allowed us to

Table 2
Image Parameters

Frequency	S_{peak} (mJy/	S_{total}	S_{rms} (mJy/	P_{peak} (mJy/	$P]_{total}$ (mJy/	P_{rms} (mJy/
(GHz)	beam)	(mJy)	beam)	beam)	beam)	beam)
(1)	(2)	(3)	(4)	(5)	(6)	(7)
15	3281	3975	7	40	50	1
22	1184	2380	7	20	30	93
22[a]	1278	2563	2	20	30	15
22[b]	300	2530	5	…	…	…
43	4510	5503	15	260	280	16
86	3460	5051	13	330	460	30

Note.
[a] All images have been obtained using uniform weighting except for this one, for which natural weighting was used.
[b] Over-resolved image of OJ 287. Columns from right to left: (1) Observing frequency, (2) Peak flux density, (3) Total flux density, (4) Noise level, (5) Peak of linearly polarized flux density, (6) Total linearly polarized flux density, (7) Noise level in the polarization image.

characterize the central compact region of the jet down to parsec-scale. The cross-identification of the individual components across epochs and frequencies was based on consistency of their positions, flux densities, and sizes. The uncertainties of the component parameters are estimated using the measured rms noise in the respective images and the S/N of detection of individual components (see Fomalont 1999; Schinzel et al. 2012; Pötzl et al. 2021, for details). All of the modelfit components are described in Table 3 and displayed in Figure 4.

3. Results

3.1. Space and Millimeter-VLBI Images of OJ 287

3.1.1. Total Intensity

Figure 4 shows the ground array (left panels) and Radio-Astron space VLBI images (right panels) of OJ 287 taken between 2014 April and May, providing a detailed view of the jet at different spatial scales.

The 15 GHz image (upper-left panel in Figure 4) shows a bright VLBI core and a one-sided jet that extends toward the west, followed by a strong jet bending by about 55° toward the southwest. The core region is modeled by a single Gaussian component labeled as C (upper-left frame in Figure 4), considered as the positional reference for the remaining modelfit components. At higher frequencies, this region is resolved into two subcomponents, C1 and C2, of the core and an extra jet component, J6 (see Figure 4).

At 22, 43, and 86 GHz images, the modelfit component C1 is considered to be the reference point. In the over-resolved RadioAstron image, the knot C1 can be further resolved into two subcomponents, C1a and C1b (lower-right panel in Figure 4). We note that the sum of the flux densities of C1a and C1b components approximately adds to that of component C1 (see Table 3).

The progressively higher angular resolution obtained with the VLBA-BU-BLAZAR 43 GHz image (middle-left panel in Figure 4), and GMVA 86 GHz image (lower-left panel) allows us to map the innermost regions of the VLBI core area up to an angular resolution of about 40 μas. This reveals that the jet bending observed at 15 GHz continues as we probe deeper into the VLBI core, from the west jet direction observed at 15 GHz to

the northwest jet direction visible at 86 GHz. The jet curvature at these spatial scales has also been reported by Hodgson et al. (2017), and is clearly imprinted here as well in the position angle of the model fitted components listed in Table 3. The position angle of the innermost component rotates from $-58°.4 \pm 0°.4$ for component J5 at 15 GHz, to $-18°.4 \pm 1°.4$ for C2 at 43 GHz, and finally $-8°.1 \pm 1°.1$ for component C2 at 86 GHz.

Our space VLBI images of OJ 287 (right panel in Figure 4) confirm that this progressive jet bending with increasing angular resolution continues up to the smallest scales probed by RadioAstron. At these extremely high angular resolutions, the core area can be resolved into two distinct components: C1a and C1b. Assuming that the upstream end of the jet characterized by component C1a corresponds to the VLBI core, the innermost jet depicted by the RadioAstron images shows a counterclockwise rotation from $-11°.7 \pm 1°.0$ for C2 to $13°.1 \pm 0°.4$ for component C1b, as we probe deeper into the upstream jet.

Downstream from the core region, the jet structure is well represented by up to six Gaussian components, labeled J1 through J6 (see Figure 4). Except for the outermost component J1, all other jet components are cross-identified at multiple frequencies.

We note here that one can try to decompose the 15 GHz flux density of the component C (3.1 Jy) into contributions from C1 and C2 by calculating their spectral indices between 22 GHz and 43 GHz and using them to estimate their respective flux densities at 15 GHz. This procedure yields the following estimates: $S_{15GHz,C1} = 0.2$ Jy and $S_{15GHz,C2} \approx 1.0$ Jy. Taken together, they sum up to 1.2 Jy, which is about 1.9 Jy less than the flux density actually measured at 15 GHz for the component C. This discrepancy most likely results from the fact that the 22 GHz RadioAstron observations were made 29 days before the 43 GHz observation and 31 days before (see Figure 5 and Section 3.3), where OJ 287 was in a lower flux density state. As OJ 287 was undergoing the rising stage of a flare during this period (see Section 3.2), the discrepancy of 1.9 Jy between the estimated and measured flux density at 15 GHz suggests that the 22 GHz flux density of one or both components (C1 and C2) blended at 15 GHz into the single component C has increased during this period.

The fitted flux densities and sizes of the modelfit components were used to calculate also the brightness temperature of each VLBI knot in the rest frame of the source (e.g., Pushkarev & Kovalev 2012):

$$T_b = 1.22 \times 10^{12} \frac{S}{\theta_{obs}^2 \nu^2} (1 + z) \ (K), \qquad (1)$$

where S is the component flux density in Jy, θ_{obs} is the size of the emitting region in milliarcseconds, ν is the observing frequency in GHz, and z is the source redshift. For unresolved modelfit components, we set $\theta = \theta_{min}$, where θ_{min} is the resolution limit (Lobanov 2005) obtained for the respective component, and consider the resulting estimate of T_b as a lower limit. The brightness temperatures estimated using this procedure are given in Column 9 of Table 3.

3.1.2. Polarization

Linear polarization is detected in all of our images in Figure 4, with the exception of the over-resolved RadioAstron image. Table 4 summarizes the linear polarization properties of the model fitted components, whereas in Appendix A.3 we
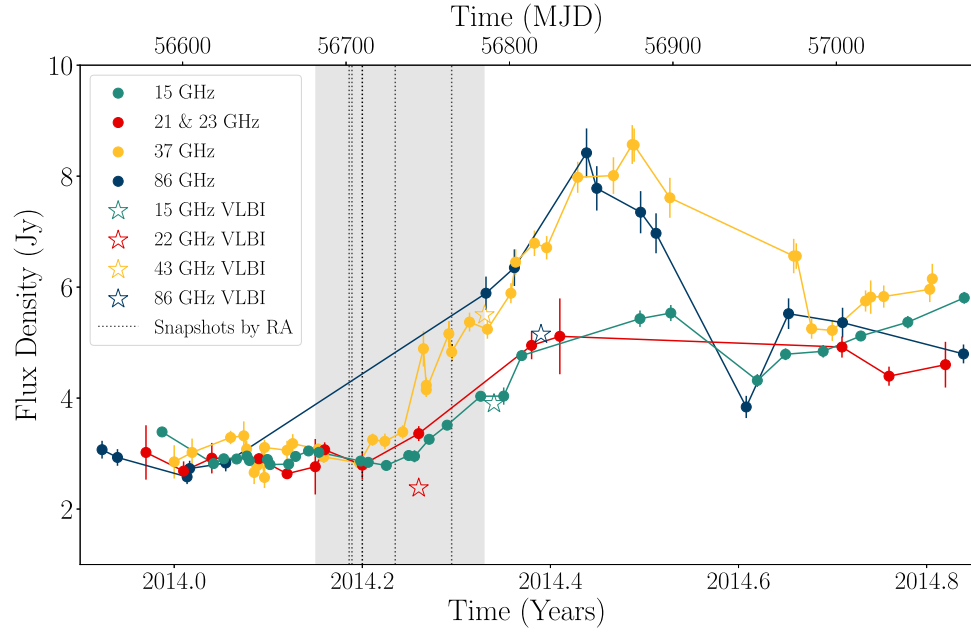
Figure 5. Single-dish (circles) flux density multifrequency measurements. During our observing interval, a prominent flaring event took place, initiated by increased γ-ray activity, displayed by the shadowed, vertical area. The dotted vertical lines designate the long-baseline RadioAstron snapshot sessions, whereas the open stars represent the VLBI observations.

Table 3
Model-fitting Parameters of OJ 287 during 2014 April–May

Knot Name (1)	Sub-knot Name (2)	Sub-knot Name (3)	Freq. (GHz) (4)	S (mJy) (5)	r (µas) (6)	PA (°) (7)	FWHM (µas) (8)	T_b (10^{10} K) (9)
C	⋯	⋯	15	3100 ± 220	0 ± 45	⋯	65 ± 5	520 ± 93
	C1	⋯	22	520 ± 110	0 ± 20	⋯	29 ± 10	205 ± 130
	C1	⋯	43	3170 ± 370	0 ± 30	⋯	<30	>270
	C1	⋯	86	1050 ± 320	0 ± 30	⋯	23 ± 10	43 ± 34
		C1a	22	120 ± 60	0 ± 15	⋯	20 ± 15	99 ± 180
		C1b	22	440 ± 100	40 ± 10	13 ± 10	21 ± 15	330 ± 535
	C2	⋯	22	1170 ± 160	100 ± 15	−12 ± 9	70 ± 40	79 ± 92
	C2	⋯	43	1530 ± 260	70 ± 40	−18 ± 31	<45	>63
	C2	⋯	86	2930 ± 510	90 ± 15	−8 ± 45	20 ± 5	160 ± 90
J6	⋯	⋯	22	360 ± 90	260 ± 30	−38 ± 6	80 ± 55	19 ± 26
J6	⋯	⋯	43	710 ± 180	190 ± 70	−45 ± 20	130 ± 50	4 ± 3
J6	⋯	⋯	86	890 ± 290	200 ± 45	−36 ± 13	114 ± 150	1 ± 4
J5	⋯	⋯	15	500 ± 90	320 ± 115	−58 ± 20	<140	>18
J5	⋯	⋯	22	220 ± 70	450 ± 55	−59 ± 7	150 ± 190	3 ± 8
J5	⋯	⋯	43	210 ± 100	430 ± 150	−51 ± 19	170 ± 100	0.6 ± 0.9
J5	⋯	⋯	86	120 ± 130	470 ± 205	−61 ± 24	163 ± 415	0.1 ± 0.5
J4	⋯	⋯	15	230 ± 60	860 ± 230	−85 ± 15	590 ± 330	0.5 ± 0.6
J4	⋯	⋯	22	140 ± 60	1000 ± 200	−79 ± 11	460 ± 1840	0.2 ± 2
J4	⋯	⋯	43	150 ± 90	1020 ± 345	−82 ± 19	510 ± 810	0.05 ± 0.2
J3	⋯	⋯	15	80 ± 40	1590 ± 355	−100 ± 13	400 ± 205	0.4 ± 0.4
J3	⋯	⋯	22	50 ± 40	1330 ± 195	−109 ± 8	230 ± 540	0.3 ± 2
J2	⋯	⋯	15	30 ± 30	2210 ± 610	−102 ± 15	<550	>0.07
J2	⋯	⋯	22	40 ± 40	1920 ± 295	−127 ± 9	306 ± 990	0.1 ± 0.9
J1	⋯	⋯	15	50 ± 30	3400 ± 560	−126 ± 9	630 ± 490	0.09 ± 0.2

Note. Columns from left to right: (1–3) Component/subcomponent ID, (4) Observing frequency, (5) Flux density, (6) Radial distance from the core, (7) Position angle, (8) Component size, and (9) Brightness Temperature (source frame).

Table 4
Polarization Properties of the Modelfit Components of OJ 287 during 2014
April–May

Knot Name (1)	Freq. (GHz) (2)	m % (3)	χ (°) (4)
P_C	15	1.2 ± 0.4	-22.5 ± 0.7
P_{C1}	22	1.5 ± 0.5	-35.4 ± 5.6
	43	8.2 ± 0.8	-16.2 ± 5.0
	86	20.9 ± 3.3	-23.4 ± 7.0
P_{C2}	22	1.0 ± 0.6	-24.18 ± 5.6
	43	15.9 ± 1.6	-17.5 ± 5.0
	86	10.4 ± 1.3	-20.5 ± 7.0
P_{J6}	22	1.1 ± 0.6	17.6 ± 5.6
	43	6.3 ± 0.6	-20.7 ± 5.0
	86	5.8 ± 4.0	8.9 ± 7.0
P_{J5}	15	4.8 ± 1.1	-8.9 ± 1.3
	43	5.8 ± 0.6	-7.6 ± 5.0
P_{J4}	15	3.0 ± 0.5	-83.9 ± 1.0
P_{J3}	15	7.5 ± 1.6	-79.5 ± 0.8

Note. The components are presented in order of increasing distance from the reference point of each image. The columns from left to right: (1) Component ID, (2) Observing frequency, (3) the degree of linear polarization, and (4) the EVPA.

present the polarization error estimation method that we followed. As it is commonly found in VLBI imaging, there is not a one-to-one correspondence between the components seen in total intensity and linear polarization. Hence, while the model fitting for total intensity is performed in the visibility plane, the two-dimensional distribution of the fractional polarization and the electric vector position angle (EVPA) for each knot are calculated in the image domain, based on the amount of polarized emission inside the area of each component. The polarization structure at 15 GHz consists of a low polarized (m $\sim$ 1.2%) core with EVPAs in the direction of the innermost jet, and polarized emission in the extended jet between model fitted components J4 and J3. Our characterization of the polarized emission in the jet as components P_{J4} and P_{J5} (see Table 4) shows an increased degree of polarization with respect to that of the core from 3% to 7.5%, as expected in the case of lower opacity, and polarization vectors aligned with the local jet direction. As discussed below in Section 3.6, the observed EVPAs are not severely affected by Faraday-rotation effects, from which we can conclude that the VLBI core and jet in OJ 287 are characterized by a dominant toroidal magnetic field component.

The linearly polarized emission at 43 and 86 GHz shows a progressive increase in degree of polarization with observing frequency in the core, reaching m $\sim$ 21% at 86 GHz, which is consistent with a transition from an optically thick core at 15 GHz to optically thin at 86 GHz, as discussed in more detail in Section 3.3 below, and may be also affected by beam depolarization (Burn 1966). The emission downstream of the VLBI core area at 43 and 86 GHz, characterized as components P_{J5} and P_{J6}, shows EVPAs predominantly oriented perpendicular to the local jet direction, and a higher degree of polarization than what is observed farther downstream in the jet area corresponding to components P_{J4} and P_{J3} at 15 GHz. This

suggests that the jet area of P_{J5}, and maybe the region between components P_{J5} and P_{J6} as well, may correspond to a recollimation shock that compresses the magnetic field in the direction of the jet, explaining the different EVPAs. However, we should also note that according to numerical simulations (e.g., Fuentes et al. 2018, 2021; Moya-Torregrosa et al. 2021), the observed net polarization in recollimation shocks can change significantly depending on the underlying magnetic field configuration, viewing angle, and other jet parameters. Alternatively, as mentioned in Sasada et al. (2018), the observed polarization may be originated by an oblique shock located where the jet bends to the west.

Alternatively, as suggested by Fuentes et al. (2018, 2021), EVPA depends on the helical magnetic field pitch angle. Lastly, is it worth mentioning that the jet presents a bend in that location, so it could correspond to an oblique shock (Sasada et al. 2018).

A higher degree of magnetic field ordering is expected in the shocked plasma, which would also explain the higher degree of polarization in this region (Jorstad et al. 2007; Hovatta et al. 2016).

The space VLBI RadioAstron images from the perigee imaging (top and middle right panels in Figure 4) show low degrees of linear polarization in the core area corresponding to components C1 and C2, with values of the order of 1% (see Table 4), and EVPAs aligned with the local direction of the jet. These low degrees of polarization are expected for optically thick emission, in agreement with what was observed at 15 GHz. The EVPAs are also in concordance with a predominant toroidal magnetic field, or a helical magnetic field with a large pitch angle. The natural weighted image (top right panel in Figure 4) shows weakly polarized emission in the area associated with component J6, with EVPAs perpendicular to the local jet direction, providing further support for the possibility that this corresponds to a recollimation shock. The measured degree of polarization for component P_{J6} is smaller than that observed at lower frequencies, which suggests that this component may be also affected by opacity effects at 22 GHz. Polarization information is resolved out in the over-resolved RadioAstron image (lower-right panel in Figure 4).

3.2. Flaring Activity of OJ 287 during 2014

OJ 287 showed multiwavelength flaring activity during 2014 April–May, coincident with our VLBI imaging campaign, as shown in the light curves of Figure 5. The event started at high energies, with γ-ray emission rising on 2014 February 25 (shadowed area in Figure 5). For the complete γ-ray light curve, see the VLBA-BU-BLAZAR website[23]. A local optical V-band maximum was reported on March 31 (Ganesh et al. 2014), followed a few days later by a flux density increase by almost $\sim$270% from the flux density level recorded between January and February, as measured by single-dish observations at 21, 23, 37, and 86 GHz. According to Weaver et al. (2021, submitted) this flare is associated with the appearance of new features in the OJ 287 jet. The quasi-simultaneous to the VLBI observations light curves were provided by the 40 m telescope of the Owens Valley Radio Observatory (OVRO) at 15 GHz (Richards et al. 2011), the RATAN-600 radio telescope at 5, 8, 11, and 22 GHz (Kovalev et al. 1999, 2002), the F-Gamma multifrequency monitoring program (Angelakis et al. 2019) at

---

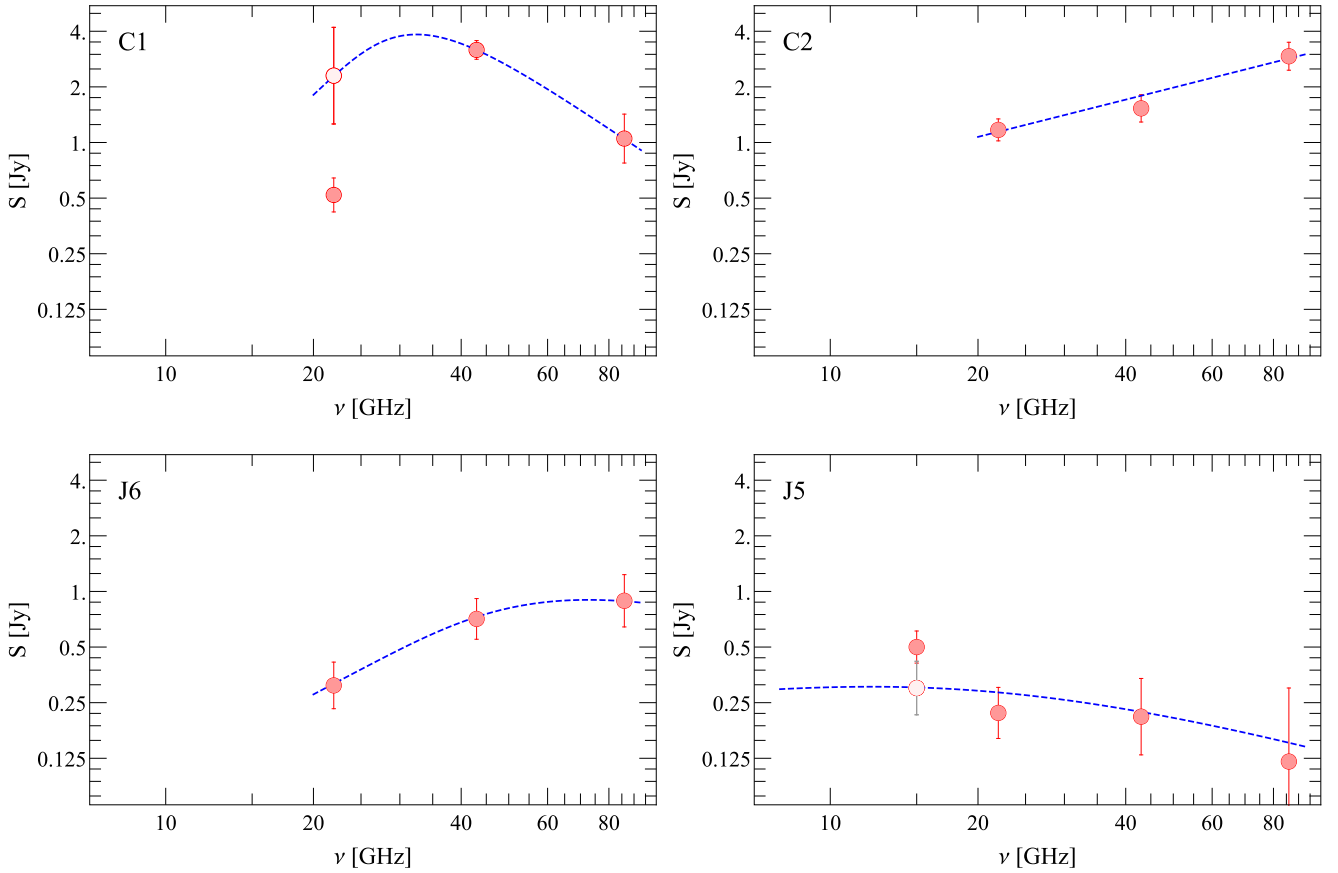[23] http://www.bu.edu/blazars/VLBA_GLAST/oj287.html

Figure 6. Observed spectra of the jet components C1, C2, J5, and J6 and best-fit models to the spectra presented in Table 5. White circles represent flux densities corrected for the source variability at 22 GHz (component C1) and for the blending effect due to the limited resolution at 15 GHz (component J5).

23 GHz, the monitoring project of extragalactic radio sources by Metsähovi Radio Telescope (Teraesranta et al. 1998) at 37 GHz, and the POLAMI monitoring program[24] at 86 GHz (Agudo et al. 2018b, 2018a).

We note that the non-simultaneity of VLBI data acquisition under such flaring conditions can introduce a big uncertainty to the spectral index estimation and the Faraday-rotation analysis results, discussed in Section 3.3 and Section 3.6.

3.3. Spectral Analysis

The quasi-simultaneous multifrequency observations in 2014 April–May enable us to analyze the spectral properties of the OJ 287 jet from parsec to sub-parsec scales during its flaring activity. For this analysis, we consider the spectrum, $S(\nu)$, of synchrotron self-absorbed (SSA) emission from a homogeneous spherical region filled with relativistic electron-positron plasma with a power-law energy distribution of emitting particles (Türler et al. 2000):

$$S_\nu = S_m \left(\frac{\nu}{\nu_m}\right)^{\alpha_t} \frac{1 - \exp[-\tau_m(\nu/\nu_m)^{\alpha-\alpha_t}]}{1 - \exp(-\tau_m)} \quad [\text{Jy}], \qquad (2)$$

where S_ν is the observed flux density in Jy, ν_m is the turnover frequency in GHz, S_m is the turnover flux density in Jy, $\tau_m \sim 3/2[(1 - (8\alpha/3\alpha_t))^{1/2} - 1]$ is the optical depth at ν_m, and α_t and α are the spectral indices of the optically thick and

thin parts of the spectrum, respectively (using the $S_\nu \propto \nu^\alpha$ definition of spectral index).

In our data, crude estimates of the synchrotron turnover point can be made for four components (C1, C2, J6, and J5) by using the Equation (2) and making an assumption about one of the two spectral slopes. As the 22 GHz observation with RadioAstron (epoch $t_1 = 2014.258$, in further discussion) preceded the observations at other frequencies by up to 50 days, we attempt to account for the potential effect of source variability by estimating the 22 GHz flux density at the epoch of May 14 (epoch $t_2 = 2014.368$, hereafter) situated in the middle of the time period between the VLBI observations at 43 GHz and 86 GHz.

At the epoch t_1 of the RadioAstron observation, a total flux density $S_{t1} = 2.98 \pm 0.04$ Jy was measured at the Effelsberg 100-m telescope. For the epoch t_2, we use the Gaussian process predictor with the 21–23 GHz measurements shown in Figure 5 to estimate $S_{t2} = 4.84 \pm 0.07$ Jy. Hence the 22 GHz emission of OJ 287 should have increased by about 1.8 Jy between the two epochs.

To decide on the most plausible distribution of the estimated 1.8 Jy increase of $S_{var,22}$, we inspect the component spectra obtained using the actually measured flux densities (see Figure 6). This inspection suggests that the 22 GHz flux densities of the components C1 is the most likely to be affected by the variability between the epochs t_1 and t_2. Its flux density at the epoch t_2 should have then increased to ≈ 2.3 Jy. If we use this value to repeat the 15 GHz flux density decomposition of the core component C discussed in Section 3.1.1, we obtain

$S_{15\text{GHz,C1}} \approx 1.9$ Jy. The respective estimated flux density of the component C then becomes ≈ 3.1 Jy, which is in excellent agreement with the actually measured flux density of this component. This agreement further supports the suggestion that the variability observed at 22 GHz between the epochs t_1 and t_2 can be ascribed to flux density changes of the component C1 in the core region. We therefore apply this assumption for the spectral fitting described below.

A clear peak in the spectrum is observed only in the component C1, while the component J6 has a rising spectrum, and the component J5 has a falling spectrum. For the component C2, the observed spectrum does not warrant estimating the turnover point, and crude limits on S_m and ν_m can be provided by the component flux density measured at 86 GHz. If we assume that the turnover flux density of C2 is similar to that of C1, then the turnover frequency of C2 should be ≈ 115 GHz. For the component J6, the measured flux densities can be used for estimating S_m and ν_m only if an assumption is made about the spectral index α of the optically thin part of the spectrum. We assume $\alpha = -0.7$ for this component. For the component J5, the 15 GHz flux density is likely to be affected by blending with the component J6 upstream. We estimate this blend to contribute ≈ 0.2 Jy to the flux density of J5, and we correct for this blend before fitting the spectrum. The fit is then done with an assumption of $\alpha = -0.8$ derived from the spectral index measured for J5 between 43 and 86 GHz. The resulting overall constraints for the component spectra and the best-fit models are presented in Table 5. The fits are also plotted in Figure 6.

Results of the spectral fitting indicate an unusual spectral evolution, with the turnover frequency first rapidly rising downstream from the component C1 (with $\nu_m > 86$ GHz in the component C2) and then falling back. Such a behavior can be explained by relativistic shocks undergoing a transition from Compton- to synchrotron-dominated emission regime (Marscher 1990), although reaching viable conclusions on this matter requires taking into account the acceleration of the emitting plasma (Lobanov & Zensus 1999).

3.4. Magnetic Fields and Equipartition Doppler Factors

The estimated turnover frequencies and flux densities of the jet components can be used for calculating their respective magnetic field strengths and Doppler boosting factors. The magnetic field strength of a spherical emitting region with an SSA spectrum is given by Marscher (1983):

$$B_{\text{ssa}}[\text{G}] = 10^{-5} b(\alpha) \, \theta_m^4 \, \nu_m^5 \, S_m^{-2} \frac{\delta_j}{1+z}, \quad (3)$$

where $b(\alpha)$ is a coefficient depending on the spectral index (with $b(\alpha) = 3.2$ for $\alpha = -0.5$; see Table 1 in Marscher 1983 and Appendix A in Pushkarev et al. 2019), ν_m is the spectral turnover frequency in GHz, S_m is the spectral turnover flux density in Jy, θ_m is the diameter of the emitting region in milliarcseconds, and δ_j is the Doppler boosting factor.

The turnover parameters, S_m and ν_m, are taken from the spectral fits in Table 5. The diameters of the emitting regions should be obtained from measurements made at the turnover frequency. In lieu of such measurements, we estimate these diameters by requiring them to reconcile the fitted turnover parameters with the maximum value of brightness temperature listed for a given feature in Table 3. For this purpose, we first

Table 5
Spectral Properties of Selected Jet Components

Comp. I.D.	α_t	α	S_m (Jy)	ν_m (GHz)
C1	$\cdots$	$\leqslant -1.6$	$\leqslant 6.0$	$\geqslant 27.4$
	2.5	-1.8 ± 0.1	3.8 ± 0.1	32.0 ± 0.1
C2	0.7 ± 0.1	$\cdots$	>2.9	>86
		$\cdots$	3.8	115
J6	1.2–2.0	$\geqslant -1.5$	0.90–0.95	65–119
	1.4 ± 0.3	-0.7	0.9 ± 0.1	71.4 ± 8.0
J5	$\cdots$	-0.8 ± 0.1	>0.5	<15
	0.2 ± 0.1	-0.8	0.3 ± 0.1	8.7 ± 0.6

Note. Spectral parameters of selected components. For each component, general constraints are given in the first row, and best model parameters are given in the second row. For the model parameters, italics denote assumed values. Column designations: α_t, α—spectral indices of the optically thick and thin parts of the spectrum, respectively; S_m—turnover flux density; ν_m—turnover frequency. For the component C2, the assumed S_m is set equal to that of the component C1, and the corresponding value of ν_m is calculated.

use Equation (1), which approximates the brightness distribution by a two-dimensional Gaussian and provides its FWHM. To obtain an estimate of θ_m, the FWHM values are further multiplied by a factor of $\sqrt{3}/\sqrt{2 \ln 2}$ accounting for the conversion from the Gaussian to the spherical shape. The conversion factor is determined by calculating the diameter of a sphere filled with homogeneous, optically thin plasma such that it provides the same total and peak flux density as those derived for a given two-dimensional Gaussian component of the modelfit. The resulting estimates of θ_m and B_{ssa} are listed in the first two columns of Table 6.

Independent estimates of magnetic field strength can be obtained from the equipartition condition (Pacholczyk 1970; Zdziarski 2014), which yields, with the same units as in Equation (3):

$$B_{\text{eq}} = 10^{-4} \left[\frac{(1 + k_u) c_{12} \, \kappa_\nu}{f} \frac{S_m \, \nu_m}{\theta_m^3 \, D_{\text{L,Gpc}}} \frac{(1+z)^{10}}{\delta_j^4} \right]^{2/7}, \quad (4)$$

where $D_{\text{L,Gpc}}$ is the luminosity distance in Gpc, f is the volume filling factor of the emitting plasma (with $f = 1$ adopted hereafter), k_u is the ratio of total energy in the emitting region to that carried by the SSA population of electrons (with $k_u \sim 1$ representing an electron-positron flow), the coefficient c_{12} is given in Pacholczyk (1970), and κ_ν depends on the low- and high-frequency cutoffs, ν_{min} and ν_{max}, of the SSA emission. For $\nu_{\text{min}} = 10^7$ Hz and $\nu_{\text{max}} = 10^{13}$ Hz assumed in this paper, the ν_{min} contribution to κ_ν can be neglected, and $\kappa_\nu \approx (\nu_{\text{max}}/\nu_m)^{1+\alpha}/(1 + \alpha)$. The resulting estimates of B_{eq} are shown in Table 6.

Both, B_{ssa} and B_{eq} depend on the Doppler boosting factor, and this dependence can be used for deriving the equipartition Doppler boosting factor, δ_{eq}, by requiring that $B_{\text{ssa}} = B_{\text{eq}}$. This condition yields $\delta_{\text{eq}} \propto (B_{\text{SSA}}/B_{\text{eq}})^{7/15}$. Using this approach, we calculate δ_{eq} and present them in Table 6 for electron-positron ($k_u = 1$) and electron-proton ($k_u = 100$; see Merten et al. 2017) jets.

The observed proper motions of the jet components in OJ 287 at 15 GHz (Lister et al. 2009, 2016) correspond to

Table 6
Estimates of Magnetic Field and Doppler Factors in the Jet

	θ_m (mas)	B_{ssa} (G)	B_{eq} (G)	δ_{eq} (e^-e^+)	δ_{eq} (e^-p)
C1	0.04	$0.002\,\delta_j$	$53\,\delta_j^{-8/7}$	103	173
C2	0.02	$>0.011\,\delta_j$	$>81\,\delta_j^{-8/7}$	<63	<105
		$0.027\,\delta_j$	$92\,\delta_j^{-8/7}$	44	75
J6	0.03	$0.24\,\delta_j$	$39\,\delta_j^{-8/7}$	11	18
J5	0.20	$0.13\,\delta_j$	$4.1\,\delta_j^{-8/7}$	5.0	8.1

Note. Column designations: θ_m—estimated effective diameter of the emitting region; B_{ssa}—magnetic field strength for synchrotron self-absorbed spectrum; B_{eq}—strength of the equipartition magnetic field; δ_{eq}—equipartition Doppler factors calculated for electron-positron (e^-e^+, $k_u = 1$) and electron-proton (e^-p, $k_u = 100$) flow, with $\delta_{eq} \propto k_u^{2/15}$. For the component C2, the second row lists respective values obtained for the assumed spectral turnover point (see Section 3.4).

apparent speeds $\beta_{app} \leqslant 15\,c$, with a median speed of $4.5\,c$, while at 43 GHz, VLBA-BU-BLAZAR monitoring have estimated values between $\sim$12c and $\sim$7c (Weaver et al. 2021, submitted). One should therefore expect to find Doppler factors $\delta_j \geqslant \sqrt{1 + \beta_{app}^2} \approx 5\text{--}15$. With this estimate, it is feasible to conclude that plasma condition in the features J6 and J5 are likely to be close to the equipartition. The components C1 and C2 in the core region deviate from the equipartition, with a good indication for this deviation to progressively increase at smaller separations from the origin of the jet.

3.5. Brightness Temperature

The highest values of T_b estimated for C1 reach $\approx 5 \times 10^{12}$ K (see Table 3). This is moderately larger than the inverse-Compton limits of $(0.3\text{--}1.0) \times 10^{12}$ K (Kellermann & Pauliny-Toth 1969) and substantially above the equipartition limit of $\approx 5 \times 10^{10}$ (Readhead 1994). At the inverse-Compton limit, a jet Doppler boosting factors $\delta_j \gtrsim 12$ would be required to explain these brightness temperature estimates. Thus, the kinematic constraints $\delta_j \approx (5\text{--}15)$ discussed Section 3.4 can reconcile the highest estimated brightness temperature values (see Table 3) with the inverse-Compton limit.

The 22 GHz modelfit estimates of T_b can be compared with the estimates of minimum brightness temperature, $T_{b,min}$, made directly from the visibility amplitudes (Lobanov 2015). This comparison is presented in Figures 2 and 7, showing that $T_{b,min}$ reaches $\approx 10^{13}$ K at the longest (u, u)-spacings coming from the auxiliary long-baseline segments of the observations.

In Figure 7, $T_{b,min}$ shows a continued increasing trend with progressive larger uv-spacing, with no evidence of reaching a plateau. Thus, even larger $T_{b,min}$ could in principle be expected at longer baselines than those observed here. Gómez et al. (2016) report $T_{b,min}$ values of the order of 10^{13} K at the longest baselines during RadioAstron observations of the jet in BL Lac at 22 GHz. The authors interpret these extremely high $T_{b,min}$ values as resulting from a flaring event that was taking place during the RadioAstron observations, causing the jet flow to depart from equipartition. Similarly, our OJ 287 observations were performed during the onset of a dramatic flaring event in the source (see Section 3.2). We should also note that the long-baseline snapshots that provide the largest $T_{b,min}$ were obtained
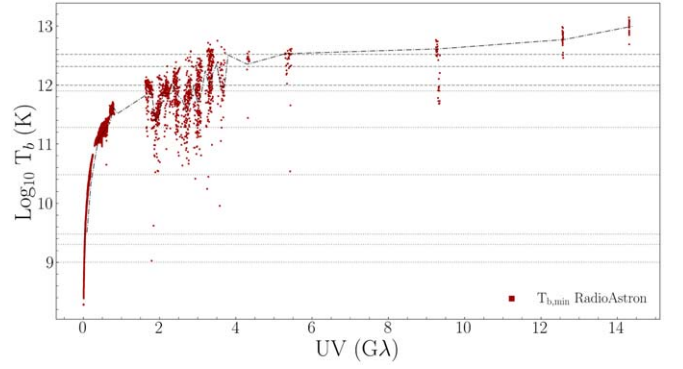

Figure 7. Brightness temperatures of modelfit components (horizontal lines) and visibility-based estimates (red dots) of minimum brightness temperature, $T_{b,min}$ in OJ 287 at 22 GHz.

during different orbits of the SRT, weeks before and after the perigee-imaging session, probing therefore probably different flaring states of the source. This provides a natural explanation for why in Figure 3 the visibilities obtained during the long-baseline snapshots do not provide a good fit to the CLEAN model obtained using only the perigee-imaging session.

The measured $T_{b,min} \sim 10^{13}$ K require Doppler boosting factors, δ_j, of the order of 10–30 to reconcile them with the inverse-Compton limit. This is broadly in agreement with the values estimated from the proper motion of components moving downstream the jet by the MOJAVE (Lister et al. 2016) and VLBA-BU-BLAZAR (Weaver et al. 2021, submitted) monitoring programs of $\delta_j \approx 5\text{--}15$ and $\delta_j = 8.6 \pm 2.8$, respectively. At the upper boundary of this range, the respective viewing angle of the jet should be $\theta_j \approx 3°\text{--}8°$. Reducing this angle by about $2^{\{°\}}$ would lead to increasing the Doppler boosting factor up to $\sim$30 even without requiring the bulk Lorentz factor to increase.

3.6. Faraday Rotation

According to theoretical models, jet launching from SMBHs is electromagnetic in nature through the action of helical magnetic fields, either anchored in the accretion disk or the BH ergosphere (Blandford & Znajek 1977; Blandford & Payne 1982). The observational signature of these fields is imprinted in the polarization information of the synchrotron radiation, and is tightly connected to the phenomenon of Faraday rotation: the rotation of the polarization plane that occurs when a polarized electromagnetic wave passes through a magnetized plasma (the so-called Faraday screen). The rotation of the polarization angle, χ, introduced by the Faraday screen is determined as $\chi = \chi_0 + RM \times \lambda^2$, where λ is the observed wavelength and χ_0 is the intrinsic electric vector position angle of the emitting region. The rotation measure (RM) is expressed by (e.g., Thompson et al. 2017):

$$RM = \frac{e^3}{8\pi^2\epsilon_0 m_e^2 c^3} \int \nu_e \boldsymbol{B}_\| d\mathbf{l}, \qquad (5)$$

where RM is measured in rad/cm^2, ϵ_0 is the permittivity of the vacuum, ν_e is the electron density, $\boldsymbol{B}_\|$ is the component of the magnetic field that is parallel to our line of sight, and $d\mathbf{l}$ is the path length from the source to the observer through the de-polarizing plasma. The sign of the Faraday rotation coincides with the sign of the line-of-sight magnetic field.
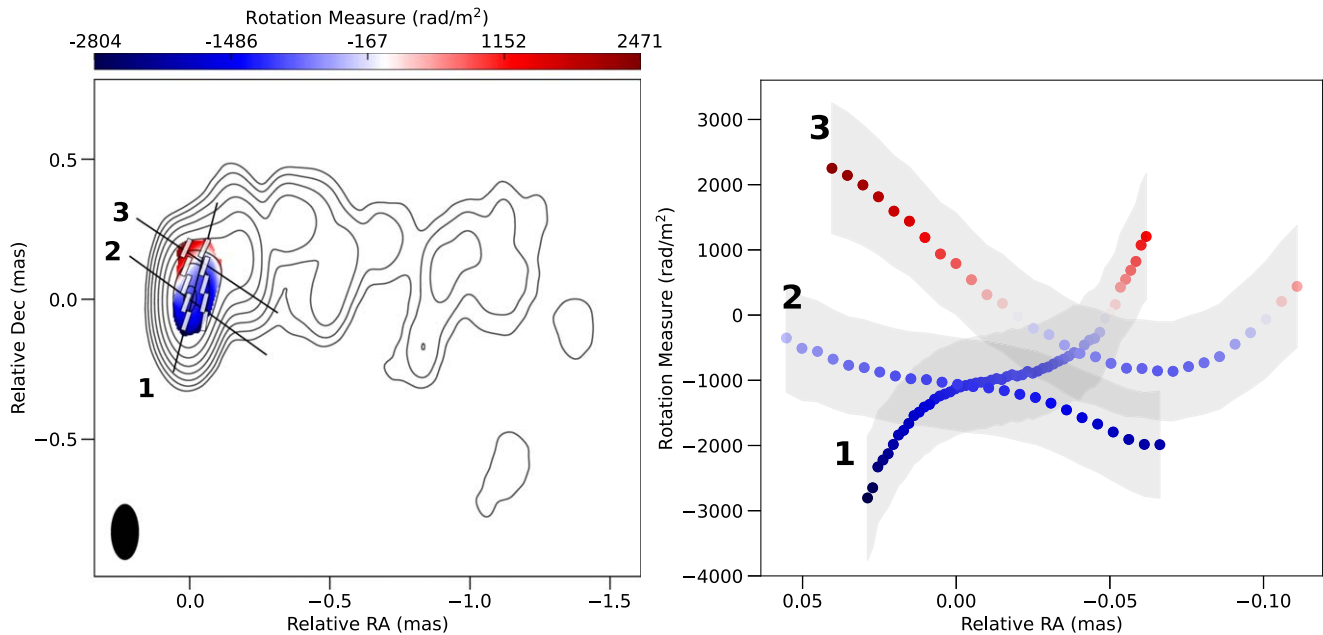
Figure 8. Left panel: rotation measure map obtained from the 22, 43, and 86 GHz images (convolved with the same 0.2×0.1 mas FWHM beam). Contours correspond to the 22 GHz image and white bars to the Faraday-corrected EVPAs. Right panel: rotation measure values along the three cuts displayed on the left panel, starting from the labeled numbers. Shaded regions indicate the profile's uncertainty.

In this work, we have combined our highest-resolution polarimetric images obtained with the ground array at 43 and 86 GHz, with that of RadioAstron at 22 GHz (natural weighted image) to produce the RM map of the innermost jet regions in OJ 287. For this we first convolved the images at the three different frequencies with a common restoring beam of 0.2×0.1 mas at a position angle of $0°$, which slightly over-resolves the 7 mm image while still preserving a fraction of the higher resolution achieved at 86 GHz and 22 GHz. Alignment of the images at the three different frequencies was obtained by performing a cross-correlation of the total intensity images following the approach described in Gómez et al. (2016), and references therein. The estimated shifts were all of the order of the image pixel size of 6 μas, and therefore no corrections were applied.

The obtained RM map, with overlaid Faraday-corrected EVPAs is shown in Figure 8. It should be noted that the images used to compute the RM were obtained at different epochs (see Table 1) during a flaring state of the source (see Section 3.2), and therefore the reliability of the obtained RM map relies on the assumption of negligible polarization structural changes in the time span covering the considered observations.

Figure 8 reveals a region with enhanced RM in the VLBI core area of OJ 287, with a median RM of -1000 ± 300 rad m^{-2}. This is broadly consistent (in magnitude) with a previous core RM estimation of -367 ± 71 rad m^{-2} based on simultaneous VLBI observations between 8 GHz and 15 GHz taken in 2006 April 28 (Hovatta et al. 2012).

The size of the RM region is of the order of our resolution beam, and therefore we lack the necessary angular resolution to accurately measure gradients in the RM (e.g., Taylor et al. 2010). With this limitation in mind, we have plotted in the right panel of Figure 8 several cuts of the RM perpendicular and parallel to the local jet direction, which are indicative for the presence of gradients across and along the jet. Gradients in RM along the jet direction are expected to be associated with a progressive decrease in the magnetic field strength and electron energy density with distance along the jet (Jorstad et al. 2007). On the other hand, gradients across the jet width are indicative for the presence of a toroidal magnetic field component. This is also consistent with the measured Faraday-corrected EVPAs, which are aligned with the local jet direction, suggesting also the presence of a predominant toroidal component in the magnetic field. The negative gradient in RM from the northeast to southwest direction suggests a toroidal magnetic field oriented clockwise as seen in the direction of flow motion.

The indicative RM gradient across the jet width and EVPAs are both in agreement with the presence of a helical magnetic field threading the innermost regions of the jet in OJ 287, as predicted by jet formation models (Blandford & Payne 1982) and observed previously in a number of sources (e.g., Gabuzda et al. 2004; O'Sullivan & Gabuzda 2009; Hovatta et al. 2012; Gabuzda 2017).

4. Discussion and Conclusions

OJ 287 is considered to be one of the best candidates for harboring a binary black hole (BBH) system in its center. The updated BBH central engine description for OJ 287 allows us to track the changes in the orientation of the accretion disk and the primary BH spin (Valtonen & Pihajoki 2013). However, additional assumptions are needed to explain its decades-long radio jet observations. Interestingly, the assumption that the jet is launched perpendicular to the innermost disk axis leads to BBH orbital timescale observational implications (Valtonen et al. 2012; Dey et al. 2021). Further, the time evolution of the innermost disk axis shows up as a bending of the radio jet. This is because the changes at the launch angle are propagated to the more distant parts of the jet with a time delay. The rather small variations of the launch angle are further amplified by projection effects since the viewing angle of the jet is small. This is in agreement with our observations, which confirm a progressive jet bending with increasing angular resolution up to the smallest spatial scales probed by RadioAstron.

Employing VLBI data sets at 15, 43, and 86 GHz, a consistent description for the temporal evolution of OJ 287 radio jet was provided in Dey et al. (2021) making use of a helicity parameter that allows for outward jet motion that is not exactly in a straight line, as noted in Valtonen & Pihajoki (2013). In addition, one may use the information of the time evolution of optical polarization and determine the jet orientation close to the jet launch site (Valtonen & Wiik 2012; Sasada et al. 2018).

In the jet distance range from 0.2 mas to 1 mas, the component position angles listed in Table 3 are in agreement with Dey et al. (2021) within the errors. For example, the position angle of component J6 is $-55 \pm 10°$ in the model while here we find $-36 \pm 13°$ (86 GHz). The optical polarization data arise from a knot at an unknown distance, but judging from the agreement of the position angle of our innermost knot C2 of the 86 GHz map and the position angle of the model (Valtonen & Wiik 2012), it is possible that the optical emission region is not far from knot C2. Beyond 1 mas, our position angle values agree with the earlier model of Valtonen & Wiik (2012).

From our BBH central engine prescription, we expect the inner components C2 and J6 to rotate counterclockwise (i.e., increasing values of position angle) by about 15° between 2014 and 2017 while the changes farther out in the jet would be barely noticeable.

Even though the observed periodicity in the light curve of OJ 287 and innermost position angle changes can be explained by a BBH model, alternative physical models can also lead to a similar phenomenology.

Britzen et al. (2018), based on 22 yr observations at 15 GHz found that the jet of OJ 287 is rotating with a period of ∼30 yr. Modeling of OJ 287 radio data showed that this rotation can be explained by a combination of jet precession and nutation. The physical cause of the precession can be driven by a binary system in OJ 287 center, as well as by the mechanism of the Lense–Thirring precession by the tilted accretion disk of a single BH (e.g., Liska et al. 2018), which in the case of OJ 287 provides realistic parameters.

Agudo et al. (2012) proposed that variable asymmetric injection of the jet flow, perhaps related to turbulence in the accretion disk, coupled with hydrodynamic instabilities leads to the non-ballistic dynamics that causes the observed nonperiodic changes in the direction of the inner jet. Cohen (2017b) presented evidence that OJ 287 is behaving as a rotating helix based on the study of MOJAVE 15 GHz VLBA images from 1995 to 2015. The results of the ridge line analysis of the data showed that the jet is rotating with a period of possibly ∼30 yr. The inner jet apparently seems to have moved to a new direction after the rotation, indicating that the jet nozzle has been re-oriented. A model of a helical jet, observed from a small and varying viewing angle, had been proposed earlier by Valtonen & Pihajoki (2013). Another suggested scenario by Hodgson et al. (2017) proposes that changes in the position angle of the jet are due to opacity shifts of the observed core in a bent jet.

On the other hand, the 12 yr periodicity of OJ 287 optical light curves, which is usually attributed to a BBH system in the center of OJ 287, can be also explained by the existence of a nonradially moving feature along a helical jet. Butuzova & Pushkarev (2020) showed that the differences between the peak flux values of the periodic optical flares, as well as the time-lag between optical and radio repeated variability, can be caused by the development of helical mode of the Kelvin–Helmholtz instability, inside a (well-aligned with our line of sight) helical jet.

Our polarization images are consistent with the innermost jet in OJ 287 being threaded by a predominantly toroidal magnetic field, while our Faraday rotation map is indicative of the presence of a gradient in RM across and along the jet. Both pieces of information suggest that the innermost jet region in OJ 287 is threaded by a helical magnetic field, as expected from jet formation models, and in agreement with previous studies. In particular, Myserlis et al. (2018) reported a clockwise EVPA rotation by ∼340° during a multifrequency single-dish campaign taken with the 100 m Effelsberg radio telescope in 2016, which is interpreted as produced by a polarized component propagating on a bent jet threaded by a helical magnetic field.

The spectral analysis combining our RadioAstron observations and ground-based VLBI observations is in agreement with the parsec-scale jet being in equipartition between the particles and magnetic field. However, there is some clear evidence for the jet being dominated by the internal energy of the emitting particles as we probe progressively closer to the central engine in the VLBI core area, in agreement with the onset of a large multiwavelength flare that peaked a few months after our VLBI observations.

Brightness temperatures have been estimated from the model fitted components, as well as from the visibility amplitudes. The maximum observed brightness temperature of 5.2×10^{12} K for the VLBI core can be reconciled with the inverse-Compton limit assuming a moderate Doppler boosting factor of the order of 5–15, in agreement with those estimated from the proper motion of superluminal components. Ground-space fringes have been detected up to a record projected baseline distance of 15.1 Earth diameters in length (one of the longest ever obtained with RadioAstron at 22 GHz), from which we have estimated a minimum brightness temperature of $T_{b,min} \sim 10^{13}$ K. The rising $T_{b,min}$ trend with projected baseline length with no indication of reaching a plateau suggests that even larger brightness temperatures could be measured with the longest baselines. Although, such extremely high-brightness temperatures could be explained by larger Doppler boosting factors than those measured at parsec scales if the innermost jet is pointing close to our line of sight. Alternatively, they may be an indication for the presence of other physical phenomena, as demonstrated by the RadioAstron observations of the quasar 3C 273 from Kovalev et al. (2016).

Further RadioAstron observations of OJ 287 have been performed in 2016, 2017, and 2018, which are also in combination with quasi-simultaneous ground-based milli-meter-VLBI observations taken with the Event Horizon Telescope (in 2017 and 2018) at 230 GHz, as well as with the Global Millimeter VLBI Array (GMVA), including phased-ALMA, at 86 GHz. These observations, together with accompanying multiwavelength coverage (Komossa et al. 2020, 2021) have the potential to either spatially resolve the hypothetical BBH system in OJ 287, or to put strong constraints on BBH and alternative models that predict the changing innermost jet position angle and overall periodic flaring activity that characterize this enigmatic source.

Appendix A
Calibration of the Instrumental Polarization

A.1. RadioAstron Data

AIPS's task LPCAL (Leppanen et al. 1995) was used to estimate the instrumental polarization leakage, also known as D-terms, independently for each IF. The target source OJ 287 was used for computing the D-terms since it was the only source observed simultaneously with the SRT while providing the best parallactic angle coverage for the ground antennas. Figure 9 shows the obtained D-terms for all of the participating antennas during the perigee-imaging session. We find consistent values across both IFs, confirming the reliability of the
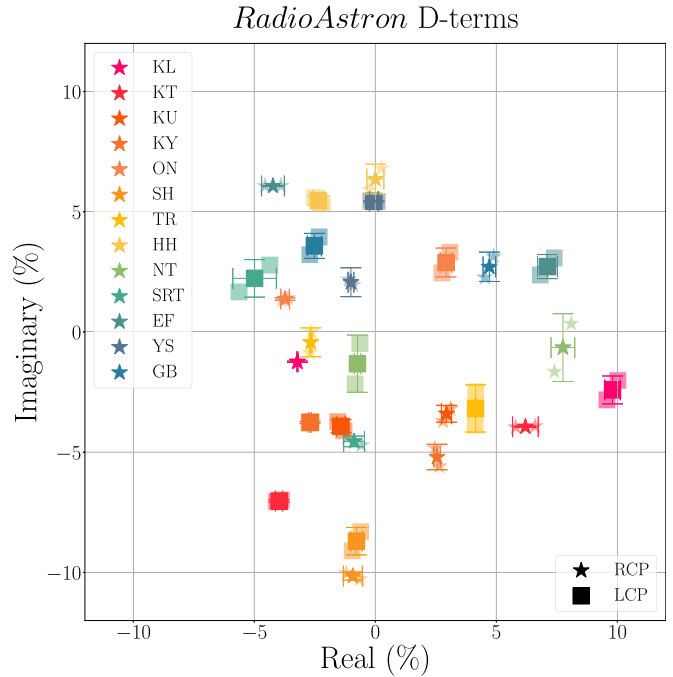
Figure 9. D-Terms for the RadioAstron perigee observations. Plotted values correspond to each IF and the median, with errors estimated from the dispersion in values across both IFs.

estimated D-terms. For the SRT, we obtained $(-0.88 - 4.55j) \pm (0.30 + 0.15j)$ and $(-4.99 + 2.23) \pm (0.63 + 0.55j)$, for RCP and LCP, respectively. The dispersion across the two IFs has been used to estimate the errors.

Absolute calibration of the EVPA was obtained through comparison with Very Large Array (VLA) observations of OJ 287 at 22.295 GHz performed in 2014 May 1 under a different observing program (Marscher et al., private communication). Given the time span between our RadioAstron observations and the VLA ones, we estimate an error for the absolute EVPA calibration, $\Delta\chi$, of the order of $10°$.

A.2. GMVA Polarization Calibration

Similarly to the RadioAstron observations, the calibration of the instrumental polarization leakage for the 86 GHz data was performed by employing AIPS' task LPCAL.

LPCAL assumes that the source structure can be described as a collection of polarization components each one with a constant fractional polarization, known as the self-similarity assumption. A good parallactic angle coverage is also required for the LPCAL fitting algorithm. Hence, ideally LPCAL should be used on sources with a simple polarization structure (preferably with a low fractional polarization), and a good parallactic angel coverage, requirements that are rarely met in millimeter-VLBI observations. Alternative methods should then be considered when these requirements are not fully met. For this reason, we have tested three different approaches to compute the D-terms for the 86 GHz GMVA observations.

First we computed the D-terms using OJ 287, which provided consistent values across all IFs, with a small dispersion of the order of $\sim2\%$ in amplitude and $13°$ in phase. Following Casadio et al. (2019), we also computed the D-terms for each one of the bright and compact sources that were observed in the same session together with OJ 287 and had a large parallactic angle coverage ($\geqslant80°$), taking the median
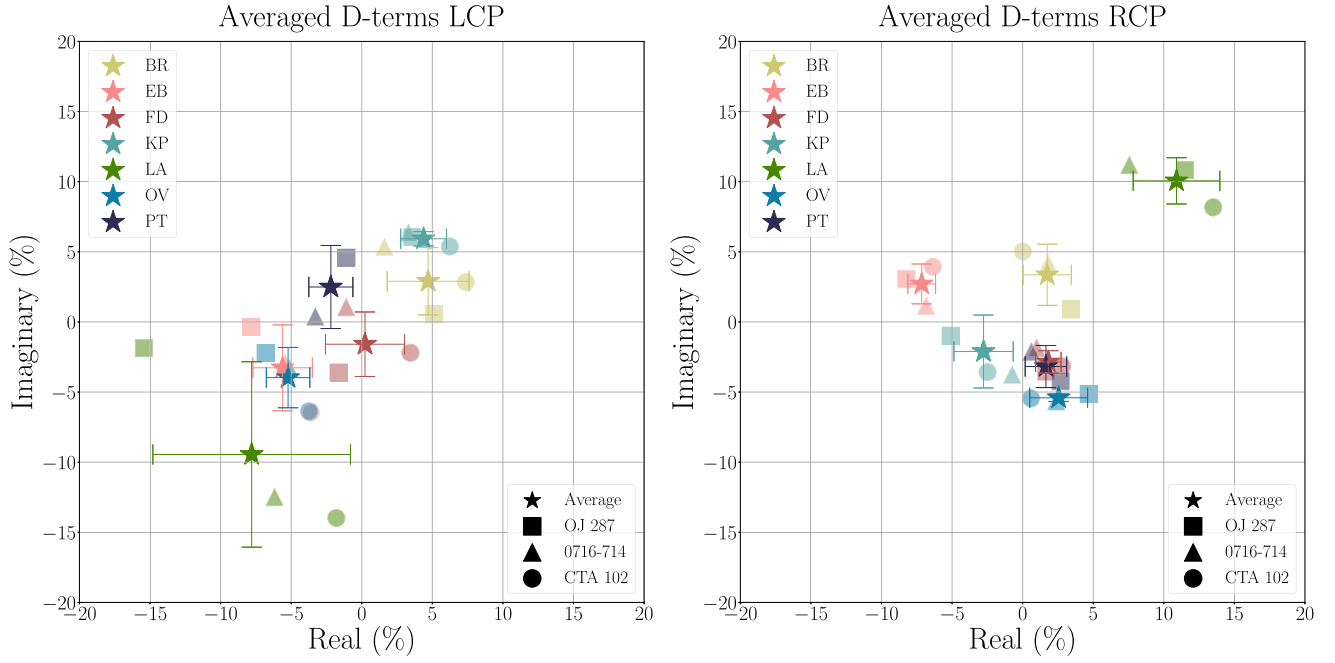
Figure 10. D-terms derived based on the data for OJ 287, 0716+714, and CTA 102, and their mean value, for the two polarizations. Labels mark the different radio telescopes. The uncertainties are estimated based on the standard deviation of the individual D-terms values.

values between the different IF channels for each antenna as the representative D-terms. Figure 10 shows the obtained D-terms for each source, including our target, and the median values. Finally we also tested which one of the D-terms obtained for each individual source provided the highest polarization image dynamic range across all observed sources. Out of these tests, we found that the D-terms provided by OJ 287 yielded the polarization image with the highest dynamic range.

Calibration of the absolute EVPA for the GMVA 86 GHz observations was carried out through comparison with the single-dish Institut de Radioastronomie Millimétrique (IRAM) 30 m telescope of OJ 287 as part of the POLAMI monitoring program, with an estimated uncertainty of the order of 5° (Agudo et al. 2018b, 2018a).

A.3. Estimations and Uncertainties of the Polarimetric Parameters

The polarized flux density in this work is computed for all data sets by the standard formula $P = \sqrt{Q^2 + U^2}$, whereas, the uncertainty of P, σ_P, is estimated by taking into account a calibration uncertainty of about 10% of the polarized flux density and a statistical error provided by the map thermal noise (Lico et al. 2014) as $\sigma_P = \sqrt{(0.1 \times P)^2 + rms_P^2}$, based on the polarization flux estimations that were obtained from the image domain of each image.

The fractional polarization percentage is determined as $m = 100(P/S)$, and the error on m is given by:

$$\Delta_m = \frac{1}{S}\sqrt{\sigma_P^2 + (m \times \sigma_S)^2 + \sigma_{D-term}^2}. \tag{A1}$$

The term σ_{D-term} represents the systematic polarization calibration error, which is defined as (Roberts et al. 1994; Hovatta et al. 2012):

$$\sigma_{D-term} = \sigma_{amp}\frac{\sqrt{S_{total}^2 + (0.3 \times S_{peak})^2}}{\sqrt{N_{ant} N_{IF} N_{scan}}} \tag{A2}$$

where σ_{amp} is the standard deviation of the D-term amplitudes, N_{ant} is the number of antennas, N_{IF} is the number of the IFs, and N_{scan} is the number of independent scans with different parallactic angles.

For the GMVA image, we have $\sigma_{amp} \sim 2\%$, $N_{ant} = 7$, $N_{scan} = 5$, $N_{IF} = 16$, $S_{peak} = 3.47$ Jy, and $S_{total} = 5.07$ Jy, which results in $\sigma_{D-term} = 4.62$ mJy/beam. Similarly, for the Radio-Astron data, we have $\sigma_{amp} \sim 1\%$, $N_{ant} = 13$, $N_{scan} = 6$, $N_{IF} = 2$, $S_{peak} = 1.18$ Jy, and $S_{total} = 2.38$ Jy, which results in $\sigma_{D-term} = 1.92$ mJy/beam. For the 15 GHz data, $\sigma_{D-term} \approx 2 \times rms_P$, and the error for the absolute EVPA calibration is of the order of 5° (Hovatta et al. 2012), whereas for the 43 GHz data, $\Delta m = 1\%$ and $\Delta \chi = 5°\%$ (Jorstad et al. 2005).

ORCID iDs

José L. Gómez ● https://orcid.org/0000-0003-4190-7613
Efthalia Traianou ● https://orcid.org/0000-0002-1209-6500
Thomas P. Krichbaum ● https://orcid.org/0000-0002-4892-9586
Antonio Fuentes ● https://orcid.org/0000-0002-8773-4933
Rocco Lico ● https://orcid.org/0000-0001-7361-2460
Guang-Yao Zhao ● https://orcid.org/0000-0002-4417-1659
Gabriele Bruni ● https://orcid.org/0000-0002-5182-6289
Yuri Y. Kovalev ● https://orcid.org/0000-0001-9303-3263
Anne Lähteenmäki ● https://orcid.org/0000-0002-0393-0647
Mikhail M. Lisakov ● https://orcid.org/0000-0001-6088-3819
Uwe Bach ● https://orcid.org/0000-0002-7722-8412
Carolina Casadio ● https://orcid.org/0000-0003-1117-2863
Ilje Cho ● https://orcid.org/0000-0001-6083-7521
Lankeswar Dey ● https://orcid.org/0000-0002-2554-0674
Leonid I. Gurvits ● https://orcid.org/0000-0002-0694-2459

Svetlana Jorstad ⓘ https://orcid.org/0000-0001-6158-1708
Yuri A. Kovalev ⓘ https://orcid.org/000-0002-8017-5665
Matthew L. Lister ⓘ https://orcid.org/0000-0003-1315-3412
Alan P. Marscher ⓘ https://orcid.org/0000-0001-7396-3332
Ioannis Myserlis ⓘ https://orcid.org/0000-0003-3025-9497
Alexander B. Pushkarev ⓘ https://orcid.org/0000-0002-9702-2307
Eduardo Ros ⓘ https://orcid.org/0000-0001-9503-4892
Tuomas Savolainen ⓘ https://orcid.org/0000-0001-6214-1085
Merja Tornikoski ⓘ https://orcid.org/0000-0003-1249-6026
Mauri J. Valtonen ⓘ https://orcid.org/0000-0001-8580-8874

References

Agudo, I., Marscher, A. P., Jorstad, S. G., et al. 2012, ApJ, 747, 63
Agudo, I., Thum, C., Ramakrishnan, V., et al. 2018a, MNRAS, 473, 1850
Agudo, I., Thum, C., Molina, S. N., et al. 2018b, MNRAS, 474, 1427
Aloy, M. A., Martí, J.-M., Gómez, J. L., et al. 2003, ApJL, 585, L109
Angelakis, E., Fuhrmann, L., Myserlis, I., et al. 2019, A&A, 626, A60
Begelman, M. C. 1998, ApJ, 493, 291
Blandford, R. D., & Königl, A. 1979, ApJ, 232, 34
Blandford, R. D., & Payne, D. G. 1982, MNRAS, 199, 883
Blandford, R. D., & Znajek, R. L. 1977, MNRAS, 179, 433
Boccardi, B., Krichbaum, T. P., Ros, E., & Zensus, J. A. 2017, A&ARv, 25, 4
Britzen, S., Fendt, C., Witzel, G., et al. 2018, MNRAS, 478, 3199
Bruni, G., Anderson, J., Alef, W., et al. 2016, Galax, 4, 55
Bruni, G., Gómez, J. L., Vega-García, L., et al. 2021, A&A, 654, A27
Bruni, G., Gómez, J. L., Casadio, C., et al. 2017, A&A, 604, A111
Burn, B. J. 1966, MNRAS, 133, 67
Butuzova, M. S., & Pushkarev, A. B. 2020, Univ, 6, 191
Casadio, C., Marscher, A. P., Jorstad, S. G., et al. 2019, A&A, 622, A158
Chiaberge, M., Celotti, A., Capetti, A., & Ghisellini, G. 2000, A&A, 358, 104
Cohen, M. 2017a, Galax, 5, 12
Cohen, M. H. 2017b, Galax, 5, 12
Daly, R. A., & Marscher, A. P. 1988, ApJ, 334, 539
Deller, A. T., Tingay, S. J., Bailes, M., & West, C. 2007, PASP, 119, 318
Dey, L., Valtonen, M. J., Gopakumar, A., et al. 2021, MNRAS, 503, 4400
EHT Collaboration, Akiyama, K., Algaba, J. C., et al. 2021a, ApJL, 910, L12
EHT Collaboration, Akiyama, K., Algaba, J. C., et al. 2021b, ApJL, 910, L13
EHTCollaboration, Akiyama, K., Alberdi, A., et al. 2019a, ApJL, 875, L1
EHTCollaboration, Akiyama, K., Alberdi, A., et al. 2019b, ApJL, 875, L2
EHTCollaboration, Akiyama, K., Alberdi, A., et al. 2019c, ApJL, 875, L3
EHTCollaboration, Akiyama, K., Alberdi, A., et al. 2019d, ApJL, 875, L4
EHTCollaboration, Akiyama, K., Alberdi, A., et al. 2019e, ApJL, 875, L5
EHTCollaboration, Akiyama, K., Alberdi, A., et al. 2019f, ApJL, 875, L6
Fomalont, E. B. 1999, in ASP Conf. Ser. 180, Synthesis Imaging in Radio Astronomy II, 180, ed. G. B. Taylor, C. L. Carilli, & R. A. Perley (San Francisco, CA: ASP), 301
Fuentes, A., Gómez, J. L., Marti, J. M., & Perucho, M. 2018, ApJ, 860, 121
Fuentes, A., Torregrosa, I., Martí, J. M., Gómez, J. L., & Perucho, M. 2021, A&A, 650, A61
Gabuzda, D. 2017, Galax, 5, 11
Gabuzda, D. C., Murray, E., & Cronin, P. 2004, MNRAS, 351, L89
Ganesh, S., Mishra, A., Chandra, S., & Baliyan, K. S. 2014, ATel, 6054, 1
Gómez, J. L., Marscher, A. P., Alberdi, A., Jorstad, S. G., & Agudo, I. 2001, ApJL, 561, L161
Gómez, J. L., Martí, J. M., Marscher, A. P., Ibáñez, J. M., & Alberdi, A. 1997, ApJL, 482, L33
Gómez, J. L., Marti, J. M. A., Marscher, A. P., Ibanez, J. M. A., & Marcaide, J. M. 1995, ApJL, 449, L19
Gómez, J. L., Lobanov, A. P., Bruni, G., et al. 2016, ApJ, 817, 96
Greisen, E. W. 1990, in Acquis., Process. Arch. Astron. Images, ed. G. Longo & G. Sedmak (Napoli: Osservatorio Astronomico di Capodimonte), 125
Hodgson, J. A., Krichbaum, T. P., Marscher, A. P., et al. 2017, A&A, 597, A80
Högbom, J. A. 1974, A&AS, 15, 417
Hovatta, T., Lister, M. L., Aller, M. F., et al. 2012, AJ, 144, 105
Hovatta, T., Lindfors, E., Blinov, D., et al. 2016, A&A, 596, A78
Jorstad, S. G., Marscher, A. P., Lister, M. L., et al. 2005, AJ, 130, 1418
Jorstad, S. G., Marscher, A. P., Stevens, J. A., et al. 2007, AJ, 134, 799
Jorstad, S. G., Marscher, A. P., Morozova, D. A., et al. 2017, ApJ, 846, 98
Kardashev, N. S., Kovalev, Y. Y., & Kellermann, K. I. 2013, arXiv:1303.5200v1
Kellermann, K. I., & Pauliny-Toth, I. I. K. 1969, ApJL, 155, L71
Komatsu, E., Dunkley, J., Nolta, M. R., et al. 2009, ApJS, 180, 330
Komissarov, S. S., & Falle, S. A. E. G. 1997, MNRAS, 288, 833
Komossa, S., Grupe, D., Parker, M. L., et al. 2020, MNRAS, 498, L35
Komossa, S., Grupe, D., Parker, M. L., et al. 2021, MNRAS, 504, 5575
Kovalev, Y. Y., Kovalev, Y. A., Nizhelsky, N. A., & Bogdantsov, A. B. 2002, PASA, 19, 83
Kovalev, Y. Y., Nizhelsky, N. A., Kovalev, Y. A., et al. 1999, A&AS, 139, 545
Kovalev, Y. Y., Kardashev, N. S., Kellermann, K. I., et al. 2016, ApJL, 820, L9
Kovalev, Y. Y., Kardashev, N. S., Sokolovsky, K. V., et al. 2020, AdSpR, 65, 705
Kravchenko, E. V., Gómez, J. L., Kovalev, Y. Y., et al. 2020, ApJ, 893, 68
Lense, J., & Thirring, H. 1918, PhyZ, 19, 156
Leppanen, K. J., Zensus, J. A., & Diamond, P. J. 1995, AJ, 110, 2479
Lico, R., Giroletti, M., Orienti, M., et al. 2014, A&A, 571, A54
Likhachev, S. F., Kostenko, V. I., Girin, I. A., et al. 2017, JAI, 6, 1750004
Lister, M. L., Cohen, M. H., Homan, D. C., et al. 2009, AJ, 138, 1874
Lister, M. L., Aller, M. F., Aller, H. D., et al. 2018, ApJS, 234, 12
Lister, M. L., Aller, M. F., Aller, H. D., et al. 2016, AJ, 152, 12
Lobanov, A. 2015, A&A, 574, A84
Lobanov, A. P. 2005, arXiv:astro-ph/0503225
Lobanov, A. P., & Zensus, J. A. 1999, ApJ, 521, 509
Lobanov, A. P., Gómez, J. L., Bruni, G., et al. 2015, A&A, 583, A100
Marscher, A. P. 1983, ApJ, 264, 296
Marscher, A. P. 1990, in Parsec-scale Radio Jets, ed. J. A. Zensus & T. J. Pearson (Cambridge: Cambridge Univ. Press), 236
Marscher, A. P. 2008, in ASP Conf. Ser. 386, Extragalactic Jets: Theory and Observation from Radio to Gamma Ray, ed. T. A. Rector & D. S. De Young (San Francisco, CA: ASP), 437
Merten, L., Becker Tjus, J., Eichmann, B., & Dettmar, R.-J. 2017, APh, 90, 75
Mizuno, Y., Gómez, J. L., Nishikawa, K.-I., et al. 2015, ApJ, 809, 38
Moya-Torregrosa, I., Fuentes, A., Martí, J. M., Gómez, J. L., & Perucho, M. 2021, A&A, 650, A60
Myserlis, I., Komossa, S., Angelakis, E., et al. 2018, A&A, 619, A88
O'Sullivan, S. P., & Gabuzda, D. C. 2009, MNRAS, 393, 429
Pacholczyk, A. G. 1970, Radio astrophysics. Nonthermal Processes in Galactic and Extragalactic Sources (San Francisco, CA: W.H. Freeman)
Petrov, L., Kovalev, Y. Y., Fomalont, E. B., & Gordon, D. 2011, AJ, 142, 35
Pötzl, F. M., Lobanov, A. P., Ros, E., et al. 2021, A&A, 648, A82
Pushkarev, A. B., Butuzova, M. S., Kovalev, Y. Y., & Hovatta, T. 2019, MNRAS, 482, 2336
Pushkarev, A. B., & Kovalev, Y. Y. 2012, A&A, 544, A34
Readhead, A. C. S. 1994, ApJ, 426, 51
Richards, J. L., Max-Moerbeck, W., Pavlidou, V., et al. 2011, ApJS, 194, 29
Roberts, D. H., Wardle, J. F. C., & Brown, L. F. 1994, ApJ, 427, 718
Sasada, M., Jorstad, S., Marscher, A. P., et al. 2018, ApJ, 864, 67
Schinzel, F. K., Lobanov, A. P., Taylor, G. B., et al. 2012, A&A, 537, 70
Shepherd, M. C. 1997, in ASP Conf. Ser. 125, Astronomical Data Analysis Software and Systems VI, ed. G. Hunt & H. E. Payne (San Francisco, CA: ASP), 77
Sillanpää, A., Haarala, S., Valtonen, M. J., Sundelius, B., & Byrd, G. G. 1988, ApJ, 325, 628
Stickel, M., Fried, J. W., & Kuehr, H. 1989, A&AS, 80, 103
Taylor, G. B., Taylor, G. B., Zavala, R., & Zavala, R. 2010, ApJL, 722, L183
Teraesranta, H., Tornikoski, M., Mujunen, A., et al. 1998, A&AS, 132, 305
Thirring, H. 1918, PhyZ, 19, 33
Thompson, A. R., Moran, J. M., & Swenson, G. W. J. 2017, Interferometry and Synthesis in Radio Astronomy (3rd edn.; Cham: Springer)
Traianou, E., Krichbaum, T. P., Boccardi, B., et al. 2020, A&A, 634, A112
Türler, M., Courvoisier, T. J.-L., & Paltani, S. 2000, A&A, 361, 850
Valtonen, M., & Pihajoki, P. 2013, A&A, 557, A28
Valtonen, M. J., Ciprini, S., & Lehto, H. J. 2012, MNRAS, 427, 77
Valtonen, M. J., & Wiik, K. 2012, MNRAS, 421, 1861
Valtonen, M. J., Zola, S., Ciprini, S., et al. 2016, ApJL, 819, L37
Weaver, Z. R., Jorstad, S. G., Marscher, A. P., et al. 2021, A&A, submitted
Zdziarski, A. A. 2014, MNRAS, 445, 1321